Geophysical Journal International

Geophys. J. Int. (2020) **221,** 1264–1280
Advance Access publication 2020 February 13
GJI Geodynamics and Tectonics

doi: 10.1093/gji/ggaa078

On formulations of compressible mantle convection

Rene Gassmöller [1,2], Juliane Dannberg [1,2], Wolfgang Bangerth [3], Timo Heister [4] and Robert Myhill [5]

[1] *Department of Earth and Planetary Sciences, University of California, Davis, Davis, CA* 95616, *USA. E-mail: rene.gassmoeller@mailbox.org*
[2] *Department of Geological Sciences, University of Florida, Gainesville, FL* 32611, *USA*
[3] *Department of Mathematics, Colorado State University, Fort Collins, CO* 80523-1874, *USA*
[4] *School of Mathematical and Statistical Sciences, Clemson University, Clemson, SC* 29631, *USA*
[5] *School of Earth Sciences, University of Bristol, Bristol BS*8 1*RL, UK*

Accepted 2020 February 10. Received 2020 February 10; in original form 2019 June 14

SUMMARY

Mantle convection and long-term lithosphere dynamics in the Earth and other planets can be treated as the slow deformation of a highly viscous fluid, and as such can be described using the compressible Navier–Stokes equations. Since on Earth-sized planets the influence of compressibility is not a dominant effect, density deviations from a reference profile are at most on the order of a few percent and using the full governing equations poses numerical challenges, most modelling studies have simplified the governing equations. Common approximations assume a temporally constant, but depth-dependent reference profile for the density (the anelastic liquid approximation), or drop compressibility altogether and use a constant reference density (the Boussinesq approximation). In most previous studies of mantle convection and crustal dynamics, one can assume that the error introduced by these approximations was small compared to the errors that resulted from poorly constrained material behaviour and limited numerical accuracy. However, as model parametrizations have become more realistic, and model resolution has improved, this may no longer be the case and the error due to using simplified conservation equations might no longer be negligible: while such approximations may be reasonable for models of mantle plumes or slabs traversing the whole mantle, they may be unsatisfactory for layered materials experiencing phase transitions or materials undergoing significant heating or cooling. For example, at boundary layers or close to dynamically changing density gradients, the error arising from the use of the aforementioned compressibility approximations can be the dominant error source, and common approximations may fail to capture the physical behaviour of interest. In this paper, we discuss new formulations of the continuity equation that include dynamic density variations due to temperature, pressure and composition without using a reference profile for the density. We quantify the improvement in accuracy relative to existing formulations in a number of benchmark models and evaluate for which practical applications these effects are important. Finally, we consider numerical aspects of the new formulations. We implement and test these formulations in the freely available community software ASPECT, and use this code for our numerical experiments.

Key words: Equations of state; Phase transitions; Mantle processes; Numerical modelling; Numerical solutions; Dynamics of lithosphere and mantle.

1 INTRODUCTION

Convection of material in the mantle of Earth and other rocky planets is understood to be a slow flow of material driven primarily by buoyancy effects caused by temperature differences. At sufficiently long timescales, the material can adequately be described as a viscous fluid, and in that case first principle considerations dictate that the flow can be described by the (compressible) Navier–Stokes equations:

$$\rho\left(\frac{\partial \mathbf{u}}{\partial t}+\mathbf{u}\cdot\nabla\mathbf{u}\right)-\nabla\cdot\tau+\nabla p=\rho\mathbf{g}, \tag{1}$$

$$\frac{\partial \rho}{\partial t}+\nabla\cdot(\rho\mathbf{u})=0, \tag{2}$$

where $\mathbf{u}$ is the velocity, p is the pressure, τ is the deviatoric stress tensor, t is time and $\mathbf{g}$ is the gravity vector. $\rho = \rho(p, T, C)$ is the density, which may depend on pressure, temperature T and chemical composition(s) C.

To first order, viscous stresses in fluids are linearly dependent on the strain rate tensor, that is, $\tau = 2\mu\left(\nabla\mathbf{u} + (\nabla\mathbf{u})^{\mathrm{T}}\right)$, where $\mu = \mu(p, T)$ is a fourth-rank tensor defined as the fluid viscosity. For isotropic fluids, μ can be reduced to two scalar components, the shear viscosity η and the bulk (or dilational) viscosity ζ, where ζ quantifies the viscous dissipation under compression or expansion. Viscous stresses in isotropic fluids can therefore be written as $\tau = \eta\left(\nabla\mathbf{u} + (\nabla\mathbf{u})^{\mathrm{T}}\right) - \left(\frac{2}{3}\eta - \zeta\right)(\nabla\cdot\mathbf{u})I$. In near-incompressible fluids, the bulk viscosity is very small (Schubert *et al.* 2001), such that the constitutive law simplifies to $\tau = 2\eta\dot{\varepsilon}$, where $\dot{\varepsilon} = \frac{1}{2}\left(\nabla\mathbf{u} + (\nabla\mathbf{u})^{\mathrm{T}}\right) - \frac{1}{3}(\nabla\cdot\mathbf{u})I$ is the deviatoric rate-of-deformation tensor. Even under these simplifying assumptions, the shear viscosity η can still depend on temperature, pressure, composition and (in the case of non-Newtonian fluids) strain rate. Our examination of the different compressibility approximations for the Stokes equations is independent of the choice of viscosity formulation, therefore, we do not further discuss any specific viscosity choice in this paper.

Eqs (1) and (2) describe processes that operate on very different timescales. Specifically, they allow for processes such as the propagation of seismic waves and the compression or expansion of material caused by dynamic pressure that operate on much shorter timescales than convection of material induced by buoyancy forces. In the following sections, we will discuss these different timescales in detail to separate timescales that are relevant to our applications from those that are not.

1.1 Timescale of seismic waves versus convective flow

While seismic waves travel on a timescale of seconds, with velocities c of the order of several kilometres per second, convective flow in the mantle occurs on timescales of millions of years, with flow velocities u of the order of centimetres per year. The ratio of these respective timescales is defined by the Mach number, $M \equiv u/c$ (Batchelor & Batchelor 2000), which is of the order of $M \approx 10^{-13}$ for the Earth's mantle. Processes on such drastically different timescales can usually not be resolved in a single numerical model. This has motivated a simplification of the equations, eliminating processes on much shorter timescales than the model time step to avoid the numerical instabilities they would cause. Specifically, studies of mantle convection typically use the infinite Prandtl number approximation, where the Prandtl number is the ratio between momentum diffusivity and thermal diffusivity, which for Earth's mantle is $\approx 10^{25}$. This eliminates the inertia term from eq. (1) (Jarvis & McKenzie 1980; Glatzmaier 1988; Bercovici *et al.* 1992). An infinite Prandtl number also implies a Mach number of zero (Curbelo *et al.* 2019), and consequently, there are no sound waves in models using this approximation.

If we neglect inertia terms, eqs (1) and (2) simplify to the following set that can be interpreted as describing force balance and mass conservation at every instant:

$$-\nabla\cdot\tau + \nabla p = \rho\mathbf{g}, \tag{3}$$

$$\frac{\partial\rho}{\partial t} + \nabla\cdot(\rho\mathbf{u}) = 0. \tag{4}$$

These equations are then augmented by an equation that describes the conservation of energy, typically expressed as an advection–diffusion equation for the temperature (see Section 2 below). In addition, if the material under consideration is chemically heterogeneous, the transport of the chemical composition needs to be considered.

1.2 Timescale of viscous relaxation versus convective flow

Even without inertia terms, eqs (3) and (4) describe processes on different timescales than that of advection (Curbelo *et al.* 2019). The time-derivative of the density in (4) introduces a different timescale, described as the *viscous isentropic relaxation timescale* $t_r = \frac{4}{3}\eta/(\gamma P_0)$ by Curbelo *et al.* (2019). Here, γ is the ratio of heat capacities at constant pressure and constant volume, and P_0 is the (constant) pressure. This timescale describes how fast regions of positive (or negative) dynamic pressure can relax by causing the material to expand (or compress) against viscous forces. In the Earth, this timescale is of the order of a few hundred years (for the upper mantle) to a few tens of thousands of years (for the lower mantle). While it is much slower than that of seismic wave propagation, it is still considerably faster than advective or conductive timescales.

Consequently, the full compressible continuity equation (4) is rarely used in analytic or computational geodynamic models. In the absence of inertia, pressures and velocities can change almost instantaneously from one time step (or one nonlinear iteration) to the next, which allows small pressure variations to cause waves in density and therefore velocity and pressure. Unless the time step of the numerical method is shorter than the viscous relaxation timescale, this causes growing pressure fluctuations and oscillations in the solution (Ismail-Zadeh & Tackley 2010; Curbelo *et al.* 2019), which may also prevent convergence of the nonlinear solver overall.

To avoid these instabilities, studies of mantle convection commonly remove the time-derivative of the density from the mass conservation equation (4) (Jarvis & McKenzie 1980; Glatzmaier 1988; Bercovici *et al.* 1992). This causes the density to respond to changes in pressure and temperature instantaneously, but does not take into account the associated volume changes (and, accordingly, does not cause flow of material). The majority of published models use one of a sequence of approximations that form a hierarchy of more simplified models; specifically, these are often referred to as the anelastic liquid approximation or ALA (Jarvis & McKenzie 1980), truncated anelastic liquid approximation or TALA (Jarvis & McKenzie 1980; Ita & King 1994) and Boussinesq approximation or BA (Oberbeck 1879; Boussinesq 1903; Rayleigh 1916). One may also add the extended Boussinesq approximation (EBA; Oxburgh & Turcotte 1978; Christensen & Yuen 1985) to this list, but since it is just a combination of the BA (for the Stokes equations) and the ALA (for the advection-diffusion of temperature), we will not further discuss it here.

All of these approximations have been instrumental in modelling mantle convection and lithosphere dynamics. They have the advantage that they (i) allow analytical solutions for simple cases; (ii) allow further analysis such as non-dimensionalized formulations that give rise to dimensionless indicators such as the Rayleigh number that characterize the flow (e.g. Rayleigh 1916); (iii) allow for computational solutions with fewer complications than the full equations. Furthermore, the ALA incorporates the first-order effects of compressibility (see e.g. Batchelor 1953; Ogura & Phillips 1962; Gough 1969), so that for many applications the model error between the choice of formulation and the exact equations may actually be smaller than the error of the numerical approximation.

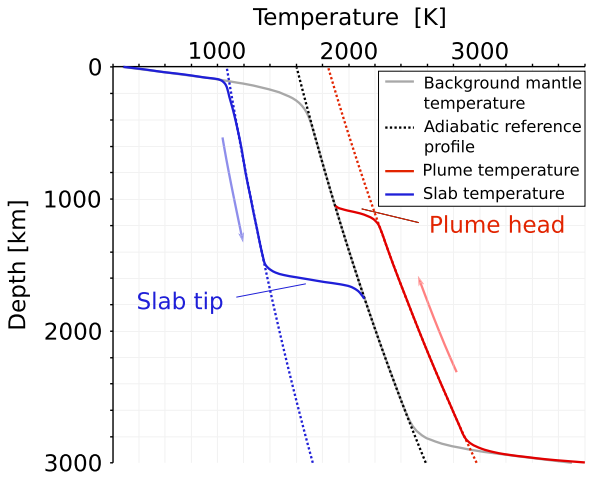

Figure 1. Many approximations to the compressible Stokes equations are based on reference profiles representing the average mantle (light-grey solid line). However, much of the energy transport in the mantle takes place within upwelling plumes (red) and subducting slabs (blue), which have temperatures (and hence, densities) that deviate substantially from this reference profile.

1.3 Importance of compressibility

Despite these advantages, all of the approximations above use some kind of 1-D reference profile—describing how density changes with depth—when computing the volumetric changes due to heating or pressurization of the material. Consequently, they do not consider how compressibility is affected when temperature, pressure, or composition deviates from that reference profile. It has been known since the 1980s that material compressibility is an important aspect in numerical simulations of mantle convection in the Earth (Jarvis & McKenzie 1980; Yuen *et al.* 1987; Steinbach *et al.* 1989; Schubert *et al.* 2001). Given the many insights our community has gained by way of computational geodynamics, using approximations such as ALA is clearly useful for many applications, and specifically for large-scale models of planetary mantle convection. On the other hand, over the last decades, the applications of geodynamic modelling codes have become substantially more complex. For example, we can now (1) use material properties computed based on mineral physics databases, leading to numerous and potentially very sharp phase transitions; (2) incorporate chemical heterogeneity, with strong variations in material properties between different rock types, specifically regarding their densities and compressibilities; (3) link different length and timescales, which places more emphasis on realistic deformation of the lithosphere and the formation of plate boundaries in convection simulations; (4) formulate multiphysics models, taking into account processes such as the seismic cycle, the generation and transport of fluids, or landscape evolution. For these applications, we know that temperatures, pressures and densities can substantially deviate from the mantle average, particularly near boundary layers, phase transitions, and due to chemical heterogeneities (see Fig. 1). In such locations, the real volume change is then substantially different from that used in the approximations above, and, consequently, so are the dynamic stresses that are important drivers of motion. For this reason, we here want to revisit the formulation of compressibility in the equations used for convection simulations.

As a first step, let us reconsider the arguments for eliminating the time derivative of the density in the mass conservation equation (4) made in Schubert *et al.* (2001). In addition to considerations regarding the different timescales, the simplification is based on the assumptions that density deviations due to temperature and other sources than the hydrostatic pressure are small (i.e. on the order of a percent or smaller). Using a linearized equation of state, and considering a density that depends on pressure p, temperature T and composition C, the corresponding density changes can be expressed as

$$d\rho = \kappa_T \rho \, dp - \alpha\rho \, dT + \Delta\rho \, dC. \tag{5}$$

Here, α is the thermal expansivity and κ_T is the isothermal compressibility (see also Section 2.2). We can estimate the contribution of each of these terms relative to the full density using typical material properties of Earth's mantle (Schubert *et al.* 2001) and assuming the largest reasonable local variations in temperature, pressure, and composition occurring in Earth's lithosphere and mantle. The pressure contribution is $\kappa_T dp \leq 3 \times 10^{-12}\,\mathrm{Pa}^{-1} \times 500\,\mathrm{MPa} = 0.15$ per cent. The temperature contribution is $\alpha dT \leq 1000\,\mathrm{K} \times 3 \times 10^{-5}\,\mathrm{K}^{-1} = 3$ per cent. The contribution of composition or phase transitions can be up to $\Delta\rho/\rho \leq 500\,\mathrm{kg\,m^{-3}}/4000\,\mathrm{kg\,m^{-3}} = 12.5$ per cent. Given these estimates, we may have to reconsider under which circumstances it is indeed appropriate to eliminate some or all of the corresponding terms from the mass conservation equation, as some density variations are not negligible compared to the total density.

To assess the effects of using the approximations described above, we therefore set out to answer the following questions:

(i) For realistic models of Earth, how accurate is each of these approximations? We will principally assess this by calculating the size of $(\partial\rho/\partial t) + \nabla\cdot(\rho\mathbf{u})$, which eq. (7) requires to be zero, but will be nonzero in the computational solutions of the approximate models, which require only $\nabla\cdot(\overline{\rho}\mathbf{u}) = 0$, where $\overline{\rho}$ is the density on the reference profile.

(ii) For realistic models of Earth, can we quantify whether the inaccuracy resulting from the assumptions actually matters? In other words, does it matter that $(\partial\rho/\partial t) + \nabla\cdot(\rho\mathbf{u}) \neq 0$, or is the violation of mass conservation acceptable because it does not result in notably different model predictions?

(iii) If there are geodynamic applications where the model error even for the most accurate commonly used approximation (namely, the ALA) is not acceptable, can we devise other approximate formulations that are more accurate? Specifically, can we find a formulation that takes into account all of the processes that are relevant for mantle convection and lithosphere dynamics, but does not include sub-time-step processes that would cause pressure oscillations? We also consider whether any such approximation can be (efficiently) implemented.

We believe that answering these questions is timely given that today's simulation codes have reached accuracies and resolutions at which the numerical approximation no longer vastly dominates the model error. Furthermore, the current generation of codes have become sufficiently sophisticated that they now have built-in parametrizations of highly complex material behaviour and are capable of incorporating more complicated compressibility formulations if our experiments show that this would be useful.

We organize the manuscript as follows. In Section 2, we introduce the governing equations and their existing approximations, and derive the new approximations we investigate in this work. In Section 3, we use several simple benchmark cases to illustrate and analyse which physical processes can and cannot be modelled by each approximation. These benchmarks also ensure that all of

the presented approximations are correctly implemented. Finally, in Section 4, we discuss several applications for which we can show that the choice of approximation matters, and these will then be the basis for the conclusions we draw in Section 5. An appendix outlines the derivation of one of our benchmarks.

2 FORMULATIONS AND APPROXIMATIONS OF THE COMPRESSIBLE STOKES EQUATIONS

In order to discuss different ways to formulate and approximate the compressible Stokes equations, let us start with the following equations describing momentum, mass, and energy conservation:

$$-\nabla\cdot\tau+\nabla p=\rho\mathbf{g}, \tag{6}$$

$$\frac{\partial\rho}{\partial t}+\nabla\cdot(\rho\mathbf{u})=0, \tag{7}$$

$$\rho C_p\left(\frac{\partial T}{\partial t}+\mathbf{u}\cdot\nabla T\right)-\nabla\cdot(k\nabla T)=\rho H+\tau:\dot{\varepsilon}+\alpha T(\mathbf{u}\cdot\nabla p)+Q_L. \tag{8}$$

The parameters in eqs (6) and (7) are the same as in eqs (1) and (2). Additionally, C_p, k, H, α, and Q_L are the specific heat capacity (at constant pressure), thermal conductivity, intrinsic specific heat production, thermal expansion coefficient, and latent heat generated by phase transitions, respectively. We allow that all of these parameters with the exception of gravity can depend on the current temperature and pressure; furthermore, we allow that the viscosity η can depend on the strain rate $\dot{\varepsilon}$ and that all parameters may also depend on the location $\mathbf{x}$ to facilitate material parametrizations that are not derived from realistic material models but incorporate *a priori* modelling assumptions. Often geodynamic models also allow for the tracking of composition or other local properties of the rock using particles/tracers or compositional fields that are advected by the velocity field, that is, solving the following equation:

$$\left(\frac{\partial C_i}{\partial t}+\mathbf{u}\cdot\nabla C_i\right)=\mathcal{R}_i \qquad \text{for } i=1\ldots n, \tag{9}$$

where n is the number of compositional quantities tracked and $\mathcal{R}_i$ are reaction rates. The dependence of parameters on $\mathbf{x}$ can then also be understood as an underlying dependence on composition C or other properties (see e.g. Heister *et al.* 2017). In other words, we consider that $\eta=\eta(p,T,\dot{\varepsilon}(\mathbf{u}),\mathbf{x})$, $\rho=\rho(p,T,\mathbf{x})$, $k=k(p,T,\mathbf{x})$, $H=H(p,T,\mathbf{x})$, $\alpha=\alpha(p,T,\mathbf{x})$, $\mathbf{g}=\mathbf{g}(\mathbf{x})$.

As mentioned above, there are numerous approximations to eqs (6)–(8) that have been widely used in the literature, such as the ALA, TALA and BA (see e.g. Bercovici *et al.* 1992, Schubert *et al.* 2001, King *et al.* 2010 and Tan & Gurnis 2007). We will discuss the assumptions and consequences of these approximations in the following subsections, and add a discussion of ASPECT's implementation of these approximations. Finally, we will derive and discuss a new approximation, which we call the projected density approximation (PDA).

2.1 Notes on phase transitions

Taking into account mineral phase transitions and their impact on material properties is essential for many problems in mantle convection.

In early studies, phase transitions were often implemented in the form of an analytical function, the 'phase function' (e.g., Christensen & Yuen 1985), which described the proportions of each stable phase in dependence of depth (or hydrostatic pressure). Usually, these functions were chosen in such a way that they provided a smooth transition from one phase to the next (such as a hyperbolic tangent), and consequently, derivatives of the density with respect to depth were easy to compute.

As geodynamic modelling codes became more complex, and thermodynamic modelling software such as Perple_X (Connolly 2005) and HeFESTo (Stixrude & Lithgow-Bertelloni 2005) became more widely used in the geodynamics community, other approaches for implementing phase transitions were developed to make use of these tools. One common approach is to use a thermodynamic modelling software and a mineral physics database to compute a table of material properties (usually with pressure and temperature as the independent variables). Every time a material property, like the density, is needed to compute the solution, this look-up table can provide its value for a known temperature and pressure (and mantle composition; e.g., Xu *et al.* 2008; Nakagawa *et al.* 2009). However, this means that the density may no longer be a smooth function on the scale of the mesh resolution used in the geodynamic model, as phase transitions may be quite sharp and appear as discontinuities when interpolated to the computational mesh. Consequently, we cannot assume any more that the density is always differentiable with respect to depth or pressure. In addition, each rock type in the model may have its own p–T–look-up table, and may follow a different equation of state.

Another possibility is to call the thermodynamic modelling software directly from the geodynamic model to compute material properties, without the intermediate step of using a look-up table. This allows for very accurate results and a wide range of chemical compositions, but is so far rarely done due to the computational cost. As in the lookup-table method above, densities and other properties may no longer be continuous in the geodynamic computation when computed externally.

2.2 Notes on thermodynamic properties

The approximations we present rely on a number of material properties to compute the density and temperature changes caused by changes in pressure, namely, the thermal expansivity, the specific heat capacity and the compressibility. While these coefficients may at first appear independent (and are treated as such in many publications), there are thermodynamic relations between these properties which must be satisfied in any self-consistent material description. In addition, it is important to distinguish between properties corresponding to isothermal (constant temperature), adiabatic/isentropic (constant entropy) and isobaric (constant pressure) processes. Specifically, we will use the following material properties:

(i) the *thermal expansivity*, describing how much the material expands due to temperature increases at constant pressure:

$$\alpha=-\frac{1}{\rho}\left(\frac{\partial\rho}{\partial T}\right)_p, \tag{10}$$

(ii) the specific *isobaric heat capacity* C_p, describing how much heat is needed to change the temperature of a given material at constant pressure:

$$C_p=\left(\frac{\partial q}{\partial T}\right)_p, \tag{11}$$

(iii) the *isothermal compressibility*, describing how much the material is compressed due to pressure increases at constant temperature:

$$\kappa_T = \frac{1}{\rho}\left(\frac{\partial \rho}{\partial p}\right)_T, \tag{12}$$

(iv) the *isentropic/adiabatic compressibility*, describing how much the material is compressed due to pressure increases at constant entropy:

$$\kappa_S = \frac{1}{\rho}\left(\frac{\partial \rho}{\partial p}\right)_S. \tag{13}$$

These properties are all second derivatives of the specific thermodynamic potentials (specific enthalpy and free energies). Consequently, there are implicit relationships between the parameters (for the derivation, see e.g. section 6.8 of Schubert *et al.* 2001), which include a relationship between the isothermal and isentropic compressibilities,

$$\kappa_S = \kappa_T - \frac{\alpha^2 T}{\rho C_p}, \tag{14}$$

and a relationship between heat capacity and the volumetric equation of state:

$$\left(\frac{\partial C_p}{\partial p}\right)_T = -T\left(\frac{\partial\,(\alpha/\rho)}{\partial T}\right)_p. \tag{15}$$

These relations also allow us to compute isentropes, which can be used as reference profiles in some of the compressibility approximations:

$$\left(\frac{\partial T}{\partial p}\right)_S = \frac{\alpha T}{\rho C_p}. \tag{16}$$

In the following case studies, we choose thermodynamic properties that ensure direct comparison between the different compressibility approximations.

2.3 The (truncated) anelastic liquid approximation

The anelastic approximation (Batchelor 1953; Ogura & Phillips 1962; Gough 1969) or more precisely its specialization for liquids, the anelastic liquid approximation (Jarvis & McKenzie 1980) is based on two assumptions. First, that lateral density variations are small relative to a reference density profile: $\overline{\rho}(r) = \rho(\overline{p}, \overline{T})$, where r is the radial or vertical coordinate, depending on whether the model is posed in spherical or Cartesian coordinates. The bar indicates that density values are taken along the reference profile, and are therefore only a function of r. The ALA approximates the density via a Taylor expansion in pressure and temperature:

$$\rho(p, T) \approx \overline{\rho}(r) + \left(\overline{\frac{\partial \rho}{\partial p}}\right)_T p' + \left(\overline{\frac{\partial \rho}{\partial T}}\right)_p T' \tag{17}$$

$$= \overline{\rho}(r)\,(1 + \overline{\kappa_T}(r)p' - \overline{\alpha}(r)T'). \tag{18}$$

Here, κ_T is the isothermal compressibility, and primes mark deviations from the reference state: $p = \overline{p} + p'$ and $T = \overline{T} + T'$.

The second assumption is that the deviation of density from the (depth-dependent) reference profile can be neglected in the mass and energy conservation equations (7) and (8), and is only considered in the right-hand side of the momentum conservation equation (the buoyancy term in eq. 6), which describes the driving force of the flow. Since this reference state is assumed to not change over time (or to only change very slowly over time), the time-derivative of the density in the mass conservation equation is zero, and eq. (7) simplifies to

$$\nabla \cdot (\overline{\rho}\mathbf{u}) = 0. \tag{19}$$

The *TALA* further simplifies the ALA by assuming that the variation of the density due to pressure variations is small, that is, that

$$\rho(p, T) \approx \overline{\rho}(r) + \left(\overline{\frac{\partial \rho}{\partial T}}\right)_p T' = \overline{\rho}(r)\,\left(1 - \overline{\alpha}(r)T'\right). \tag{20}$$

Both the ALA and TALA then use the depth-dependent $\overline{\rho}(r)$ in the energy conservation equation (8).

We note that this verbal description is not the original way in which the ALA was derived. Instead, the original derivation (Batchelor 1953; Ogura & Phillips 1962; Gough 1969; Jarvis & McKenzie 1980) is based on a non-dimensionalization of the equations and a polynomial expansion of the relevant terms, after which the higher order terms are neglected. We chose to present the approximations in the current way to make it easier to understand the physical assumptions implied by the mathematical description.

2.4 The Boussinesq approximation

Although derived more than 50 yr before the ALA, the *BA* (Oberbeck 1879; Boussinesq 1903; Rayleigh 1916) can be seen as a further simplification of the ALA that assumes a constant reference temperature and reference density, $\overline{T}(r) = T_0$, $\overline{\rho}(r) = \rho_0$. In other words, density variations are assumed to be so small that they are negligible everywhere except in the buoyancy term of the momentum equation (6). This simplifies the mass conservation equation (7) to its incompressible form $\nabla \cdot \mathbf{u} = 0$. In addition, as the reference temperature is constant, adiabatic and shear heating are not considered in the energy equation (8).

Both the BA and the ALA (approximating the behaviour of pure gases/liquids or atmospheric convection, respectively) were originally designed assuming density variations predominantly due to temperature and pressure. Nevertheless, in geodynamic modelling, they have been widely used with density variations caused by compositional heterogeneity and phase transitions. The former is justified as long as density variations due to chemical heterogeneities remain small (similar to the effect of temperature variations), or if they do not vary strongly with depth. In the Earth's mantle, this is not necessarily the case (see e.g. Tan & Gurnis 2007). Phase transitions may cause even bigger density deviations. As long as the model is isochemical, ALA/TALA implementations can include phase transitions in the background reference density profile, and they can even model the effects of a non-zero Clapeyron slope and the latent heat release or consumption by adding the corresponding terms in the temperature equation and in the buoyancy term (e.g. Christensen & Yuen 1985; Tackley *et al.* 1993; Bunge *et al.* 1997; Nakagawa & Tackley 2004; Nakagawa *et al.* 2009; Leng & Zhong 2010). However, in chemically heterogeneous models, the depth range and density change of a phase transition depends on the chemical composition, which means that it cannot be included in a single reference profile. In this case, neither BA nor ALA can be used to model the effect of volumetric contraction or expansion of at least a part of the material. Volume changes due to phase transitions can reach almost 10 per cent over very narrow depth ranges for important phase transitions in the deep mantle [e.g. at the 670 km discontinuity; *cf.* the Preliminary Reference Earth Model by Dziewonski & Anderson (1981)], and may be even larger for dehydration reactions in shallower parts of the Earth. Furthermore,

these large density gradients may not all be at the same depth as a function of temperature and composition, such that any given 'reference' profile has less physical meaning; as an example, the '410' km discontinuity is not, in fact, at a constant depth everywhere in Earth, and will not exist at all in materials devoid of olivine/wadsleyite.

2.5 New approximations

In the following, let us introduce three approximations that go beyond those discussed above. All of these start by considering why we do not want to solve the original mass conservation equation (2),

$$\frac{\partial \rho}{\partial t} + \nabla \cdot (\rho \mathbf{u}) = 0,$$

directly. Besides the fact that the equations are nonlinear, the principal difficulty is that the primary variables of the full momentum conservation equation (1) are the velocity and pressure, but in the mass conservation equation the primary variables are the density and momentum. One can resolve this by expressing the density in terms of the pressure and temperature, as done in eqs (17) and (20), for example; however, applying the product and chain rules to $\nabla \cdot (\rho \mathbf{u})$ leads to complicated terms that are difficult to discretize. As a consequence, all of the approximations described above use a reference density of some kind in the mass conservation equation. The new problem is also linear, and thus easier to solve.

But we can still ask whether the use of the chain rule can lead to a more accurate approximation. To this end, let us rewrite the mass conservation equation in the following form:

$$\frac{1}{\rho}\left(\frac{\partial \rho}{\partial t} + \nabla \cdot (\rho \mathbf{u})\right) = \frac{1}{\rho}\frac{\partial \rho}{\partial t} + \nabla \cdot \mathbf{u} + \left(\frac{1}{\rho}\nabla \rho\right) \cdot \mathbf{u} = 0. \tag{21}$$

The approximations derived below use this form as a starting point.

2.5.1 *The isentropic compression approximation (ICA)*

The ICA can be seen as a variation of the ALA and is the default for handling compressible models in the ASPECT software used for the numerical experiments in this paper. ICA follows the ALA and BA in neglecting time derivatives of the density in the mass conservation equation. It then replaces the reference density profile with an approximation of the effects of static compression due to the action of gravity at each point. This is achieved by introducing a depth-dependent reference hydrostatic pressure $\overline{p}_h = p(r)$, calculated using a 1-D density (and gravity) profile that is characteristic for the model. Using this approximation in eq. (21) results in the replacement of $\frac{1}{\rho}\nabla \rho \approx \frac{1}{\rho_h}\nabla \rho_h \approx \frac{1}{\rho_h}\frac{\partial \rho_h}{\partial p}\nabla \overline{p}_h \approx \kappa_S \rho_h \mathbf{g}$, and consequently

$$\nabla \cdot \mathbf{u} = -\kappa_S \rho_h \mathbf{g} \cdot \mathbf{u}, \tag{22}$$

where κ_S is the compressibility at constant entropy and $\rho_h = \rho(\overline{p}_h, T, C)$. Because the approximation uses the isentropic compressibility (rather than the isothermal compressibility), the right-hand side of the equation describes volume changes along an adiabat due to the combined effect of the changes in pressure and temperature.

The ICA thus has different modelling assumptions than ALA. ALA neglects all density changes that are not included in the reference profile, for example lateral variations in composition or temperature. It is possible to take into account changes in the reference profile over time, such as caused by secular cooling of the Earth, by recomputing the profile in given time intervals, but at every given instant there is only one reference profile describing how the density changes with depth. In contrast, ICA does not have one exclusive reference profile, but instead calculates the material adiabat based on the current temperature, pressure and composition (because both ρ_h and κ_S can depend on these variables). Consequently, it automatically computes an approximation to the local adiabat for material with a different composition, material with a higher or lower temperature than the average mantle such as plumes or subducted slabs, and changes in average mantle temperature over time. However, ICA still neglects the volumetric effects of local density changes over time not caused by advection along an adiabat (e.g. due to thermal diffusion or radiogenic heat production).

The ICA can be used either with a reference density profile or the full density in the temperature equation. In the benchmark experiments and applications presented in the following sections, we will use the formulation with the full density.

2.5.2 *The hydrostatic compression approximation (HCA)*

The HCA (Heister *et al.* 2017) follows a similar derivation, but approximates the gradient of the density in a different way. Specifically, it reintroduces the effects of local temperature gradients, replacing the reference density profile by the effects of static compression *and* dynamic temperature at each point. The resulting expansion is in terms of temperature and pressure (but not composition), rather than pressure at constant entropy:

$$\begin{aligned}\frac{1}{\rho}\nabla \rho &\approx \frac{1}{\rho}\left(\frac{\partial \rho}{\partial p}\nabla p + \frac{\partial \rho}{\partial T}\nabla T\right) \approx \frac{1}{\rho}\left(\frac{\partial \rho}{\partial p}\nabla \overline{p}_h + \frac{\partial \rho}{\partial T}\nabla T\right) \\ &\approx \frac{1}{\rho}\left(\kappa_T \rho(\rho_h \mathbf{g}) - \alpha \rho \nabla T\right),\end{aligned}$$

which, when entered into (21), yields

$$\nabla \cdot \mathbf{u} = -\left(\kappa_T \rho_h \mathbf{g} - \alpha \nabla T\right) \cdot \mathbf{u}. \tag{23}$$

Note that this approximation uses κ_T, the isothermal compressibility (rather than isentropic compressibility), so that $-\kappa_T \rho_h \mathbf{g} \cdot \mathbf{u}$ describes the effect of compression/expansion due to isothermal pressure changes and $\alpha \nabla T \cdot \mathbf{u}$ describes the compression/expansion due to isobaric temperature changes. As a consequence, the HCA also uses different modelling assumptions than the ALA. While the ALA neglects all effects due to deviation from the reference profile, the HCA includes the effects of pressure and temperature variations as separate contributions. As we will show this is more accurate than the ALA for steady state cases (both close to and further away from the reference profile), but cannot accurately model time-dependent flow. Consider, for example, a volume of material that contains a lateral density gradient (e.g. caused by temperature). If that material is purely advected along at constant pressure and temperature, the density of a small parcel that moves with the flow does not change, therefore the divergence of the velocity should be zero. This can be demonstrated by the Lagrangian formulation of the mass conservation equation (2):

$$\frac{D\rho}{Dt} + \rho \nabla \cdot \mathbf{u} = 0, \tag{24}$$

where $D\rho/Dt = (\partial \rho/\partial t) + \nabla \rho \cdot \mathbf{u}$ is the Lagrangian material derivative of the density. The advection of temperature (and the related density) gradients with the flow alone does not change the density along material pathlines over time (i.e. $D\rho/Dt = 0$). Accordingly, the divergence of the velocity should be zero in that case. However, eq. (23) yields $\nabla \cdot \mathbf{u} = -\alpha \nabla T \cdot \mathbf{u} \neq 0$, which is clearly wrong for this thought experiment.

We will illustrate the effect of this inconsistency in Section 3.2 and despite describing the approximation in an earlier publication (Heister *et al.* 2017) advise against using it for geodynamic computations. The HCA—just as the ICA—can be implemented to use either a reference density or the full density in the energy conservation equation.

2.5.3 The projected density approximation

Compared to the full mass conservation equation (2), both the ICA and the HCA suffer from the fact that (i) the time derivative of the density is neglected and (ii) the approximations assume that the density is differentiable with regard to the pressure and, in the case of the HCA, the temperature. This latter assumption is not valid if the density is essentially discontinuous, for example, in the presence of phase changes. In fact, applying the product rule to $\nabla \cdot (\rho \mathbf{u})$ is also not valid in that case, but we will ignore this for a moment.

The reason why we have derived approximations under these assumptions is that the density is not a primary variable in geodynamic computations, but is a function of the computed pressure and temperature fields. Consequently, we cannot express the time derivative or gradient of the density without recourse to the time derivatives or gradients of the pressure and temperature fields, using the chain rule. In the following, we will therefore pursue an entirely different strategy that does not attempt to express the density variations through pressure or temperature variations, but instead tries to stay closer to the original form by directly using the density, which then also allows us to keep the time derivative.

As mentioned in Section 1, the full compressible continuity equation is rarely used in convection models because it causes pressure oscillations in the solution (Glatzmaier 1988; Ismail-Zadeh & Tackley 2010) and convergence problems for nonlinear solvers. All of the previously discussed formulations prevent the generation of this type of pressure oscillations by using time-independent reference densities. However, as discussed, this also excludes dynamic contributions from temperature and composition. Therefore when deriving the new formulation of this section, we choose to stay close to the full density (including dynamic temperature and composition), but use a reference pressure profile $\overline{p}_h$ (as in the HCA) to prevent the generation of pressure waves. This is a more accurate approximation than made in the ALA, because density changes due to the 'dynamic pressure' $(p - \overline{p}_h(r))$ are small compared to the ones caused by local compositional heterogeneities and temperature variations (see Section 1.3). Nevertheless, there might be special cases where dynamic pressure effects exceed the influence of other variations and become important. In particular, at shallow depths (above the isostatic compensation depth), different regions may have total pressures which differ significantly from the reference hydrostatic profile. In this case, however, none of the discussed formulations will be a good approximation to the full set of conservation equations. This is not an important consideration for mantle convection or lithosphere dynamics simulations, as long as a reasonable reference pressure profile has been chosen.

Accordingly, we propose using the following form of the mass conservation equation:

$$\nabla \cdot \mathbf{u} = -\frac{1}{\rho_h}\frac{\partial \rho_h}{\partial t} - \frac{1}{\rho_h}\nabla \rho_h \cdot \mathbf{u}.$$

Unfortunately, as mentioned, we cannot evaluate the right-hand side terms because numerically only p and T are known as functions of $\mathbf{x}$ and t, and $\rho_h = \rho_h(\overline{p}_h(\mathbf{x}, t), T(\mathbf{x}, t), C(\mathbf{x}, t))$ can in general be an expression that we cannot differentiate with respect to $\mathbf{x}$ or t.

Therefore, we replace ρ_h by its projection or interpolation $\tilde{\rho}_h$ onto a finite dimensional space R_h, for example, the same space that is used to represent temperature. Then, the final version of the mass conservation equation used in the PDA is as follows:

$$\nabla \cdot \mathbf{u} = -\frac{1}{\tilde{\rho}_h}\frac{\partial \tilde{\rho}_h}{\partial t} - \frac{1}{\tilde{\rho}_h}\nabla \tilde{\rho}_h \cdot \mathbf{u}. \tag{25}$$

This formulation has a variety of advantages. First, in order to compute $\tilde{\rho}_h$ by projection or interpolation, we only need the *values* of ρ_h at individual points, but not its derivatives. Second, as an element of the finite dimensional space R_h, we know how to compute spatial and temporal derivatives of $\tilde{\rho}_h$ easily and efficiently, and so all terms on the right-hand side of (25) are easy to evaluate. And, finally, if one chooses R_h to be a space of continuous functions (e.g., one of the usual continuous finite element spaces), then the right-hand side is also always well-defined.

The formulation also solves another problem in the finite element context: If R_h is chosen as a space of continuous functions, and if the space used for the discretization $\hat{\mathbf{u}}$ of the velocity $\mathbf{u}$ is also continuous (as is typically done), then the application of the product rule in $\nabla \cdot (\tilde{\rho}_h \hat{\mathbf{u}}) = \nabla \tilde{\rho}_h \cdot \hat{\mathbf{u}} + \tilde{\rho}_h \nabla \cdot \hat{\mathbf{u}}$ is now well-defined.

In our computational practice, the way the system of (3) and (25) is solved is that we keep all terms that involve the density on the right-hand side and perform a fixed-point iteration as described in Heister *et al.* (2017). We remark that computing the time derivative of $\tilde{\rho}_h$ involves the (projected) density from previous time steps. It is natural to use the same approximation for the time-derivative as for the other time-dependent solution variables. In our implementation, we use a BDF2 approximation for the time derivative in time step n, using the solution at time steps $n-1$ and $n-2$ (see Kronbichler *et al.* 2012):

$$\frac{\partial \tilde{\rho}_h^{n,s}}{\partial t} \approx \frac{1}{k_n}\left(\frac{2k_n + k_{n-1}}{k_n + k_{n-1}}\tilde{\rho}_h^{n,s} - \frac{k_n + k_{n-1}}{k_{n-1}}\tilde{\rho}_h^{n-1,*} + \frac{k_n^2}{k_{n-1}(k_n + k_{n-1})}\tilde{\rho}_h^{n-2,*}\right).$$

Here, $k_n = t^n - t^{n-1}$ denotes the length of the nth time step and s is the number of the fixed point iteration at the current time step. Furthermore, $\tilde{\rho}_h^{n-1,*}$ is the projected density from the last nonlinear iteration in the previous time step (and similarly for $\tilde{\rho}_h^{n-2,*}$). On the other hand, $\tilde{\rho}_h^{n,s}$ is computed by projection (or interpolation) of $\rho_h(\overline{p}_h, T^{n,s}, C^{n,s})$, except in the first nonlinear iteration where it is computed by projecting (or interpolating) $\rho_h(\overline{p}_h, \hat{T}, \hat{C})$ where $\hat{T}$ and $\hat{C}$ are linearly extrapolated from the previous two time steps.

The resulting set of equations is of course more nonlinear than simpler approximations like ALA, and therefore potentially more computationally expensive. However, in our models in the following sections we observe that the additional computational cost can vary significantly, depending on other existing nonlinearities in the model. For steady-state convection benchmarks like the ones in Section 3 we observe an additional cost of less than 10 per cent. For models with strong nonlinearities, we observe a higher cost for the PDA: for example, the model of contracting crust (Section 4.3) requires twice the time for PDA, almost exclusively because of a higher number of nonlinear iterations per time step.

3 BENCHMARKS: HOW APPROXIMATING THE MASS CONSERVATION EQUATION INFLUENCES THE FLOW

After introducing the different compressibility approximations for the Stokes equation, we will now discuss their performance in simple steady-state and time-dependent benchmark models. To this end, we first introduce a number of different 1-D benchmark cases that quantify the mass error associated with each approximation. We start from the simple case of steady-state flow along an adiabat, and gradually introduce varying complexities, such as deviations from the adiabat, temperature changes over time, advecting density gradients and varying pressure over time.

The formulations and benchmark setups are implemented in the open source community code ASPECT (Kronbichler *et al.* 2012; Bangerth *et al.* 2016, 2018; He *et al.* 2017; Heister *et al.* 2017) newer than git version 41b7640f9. The specific version of ASPECT used for the models in this manuscript is available at https://github.com/gassmoeller/aspect/releases/tag/compressible-formulations-submission as git version 82e47f2fd. The input files and post-processing scripts for benchmarks and models in this manuscript are available at https://github.com/gassmoeller/formulations-of-compressible-mantle-convection-data.

3.1 1-D vertical or horizontal steady-state flow

The first model describes vertical flow along an adiabat. The setup consists of a long vertical pipe (aspect ratio 10:1), in which material is leaving the lower outlet with a prescribed velocity, driving the downward flow. The upper inlet is stress-free (open), and material enters with a constant temperature. The side boundaries are free-slip. Due to a constant downward gravity this model develops a hydrostatic pressure profile, which leads to an increase of the (compressible) material density with depth. The thermal expansivity and isothermal compressibility are chosen as constant, and the thermal conductivity is set to zero in order to let an adiabatic temperature profile develop. The heat capacity is set to be constant, consistent with the thermodynamic relations in (14)–(16) if temperature changes are adiabatic. This then leads to a density that satisfies

$$\rho(p, T) = \rho_0 \exp(\kappa_T(p - p_0) - \alpha(T - T_0)),$$

with the reference pressure $p_0 = 0$ and the reference temperature $T_0 = 1600$ K. This profile satisfies the definitions of the thermal expansivity and isothermal compressibility given in eqs (10) and (12). (The thermodynamic relations require that the isentropic compressibility cannot be constant, and we can compute it from the quantities given above using eq. (14).) There is no internal heat generation in the material except for adiabatic heating. A sketch of the model and its parameters is shown in the top left panel of Fig. 2. Under these conditions, the exact material velocity decreases as density increases with depth to create a constant mass flux. Indeed, since the setup is 1-D, the mass conservation equation (2) implies that $\rho u_z = $ constant, and the velocity is readily computed using the density profile above. This means we can quantify the error of the different formulations as the difference between the mass flux at the inlet and the outlet, normalized by the mass flux at the outlet. To illustrate the limitation of approximations that use a reference profile, we will consider two cases: (i) the material that enters has the potential temperature of the reference profile and (ii) the material at the inlet has a lower temperature than the reference profile (e.g. like a cold subducting plate would have).

The top row of Fig. 2 shows that for this test case, the various approximations have different systematic (model) errors—which are independent of the mesh resolution—and numerical (discretization) errors—which converge to zero with increasing resolution. For steady-state flow along the reference adiabat, all approximations solve the equations with similar accuracy and converge to an error of zero (Fig. 2b), because in this case the model error is zero. But because the ALA was only designed to accurately model compression at its reference adiabatic profile, it suffers from a systematic error as soon as material moves along a different adiabat. This lets the mass flux error stagnate at a relatively high level (10^{-3}, Fig. 2c), whereas the new approximations proposed in Section 2.5 converge with mesh resolution towards an error of 0, with a second-order convergence rate. The PDA shows generally the smallest mass errors of all approximations, independent of mesh resolution.

The second model setup (bottom left panel of Fig. 2) is a rotated version of the first setup, creating lateral pipe flow. Whereas the first test case was designed to capture heating due to adiabatic compression (e.g., in subducting slabs or rising plumes), in this example we test how well the different compressibility approximations can capture non-adiabatic changes in temperature (e.g., the cooling of an oceanic plate as it moves away from a mid-ocean ridge). For this purpose, we switch off gravity (to simplify the model and eliminate the density changes caused by the hydrostatic pressure), but instead introduce internal heat production in the material. Heat capacity is again set to be constant (this is thermodynamically consistent, as the conditions within the domain lie along a single line in p-T space). The internal heat production increases from the inlet to the outlet as $H = 10^{-10}e^{x/l}$ W/kg, where l is the length of the pipe, but H does not vary with time. This leads to thermal expansion over time as the material travels from the inlet (left) to the outlet (right), and we consequently expect an increase in velocity from the inlet (higher density) to the outlet (lower density). It stands to reason that approximations that assume compression only in downward direction (e.g. by relying on a depth-dependent reference profile) are not able to capture this type of situation well.

This is confirmed by the results in Fig. 2, bottom. Only the PDA and HCA have a zero model error (observed as the mesh size goes to zero), while the ALA and ICA show a stagnating model error (Figs 2d and e). Because these latter two were designed to model adiabatic volume changes, they do not capture the volume change caused by non-adiabatic temperature changes.

3.2 1-D transient flow

In the test cases above we have looked at steady-state behaviour, but in practical applications the density at each point within the domain is time-dependent, making the term $\partial\rho/\partial t$ relevant (as we will demonstrate in Sections 4.2 and 4.3). To study this effect, we have designed three time-dependent benchmarks.

As a first case, we consider an open pipe (just like in the lateral pipe benchmark above) that has an open boundary on the right, allowing free in- and outflow of material, and a closed boundary on the left. Over time, the material in the pipe is slowly heated internally. The resulting expansion causes outflow of material through the open boundary, and the amount of outflow should be equivalent to the loss of mass inside the pipe. The PDA is the only one of the formulations discussed in Section 2 that includes the time derivative of the density, so one might expect that it alone can yield accurate solutions.

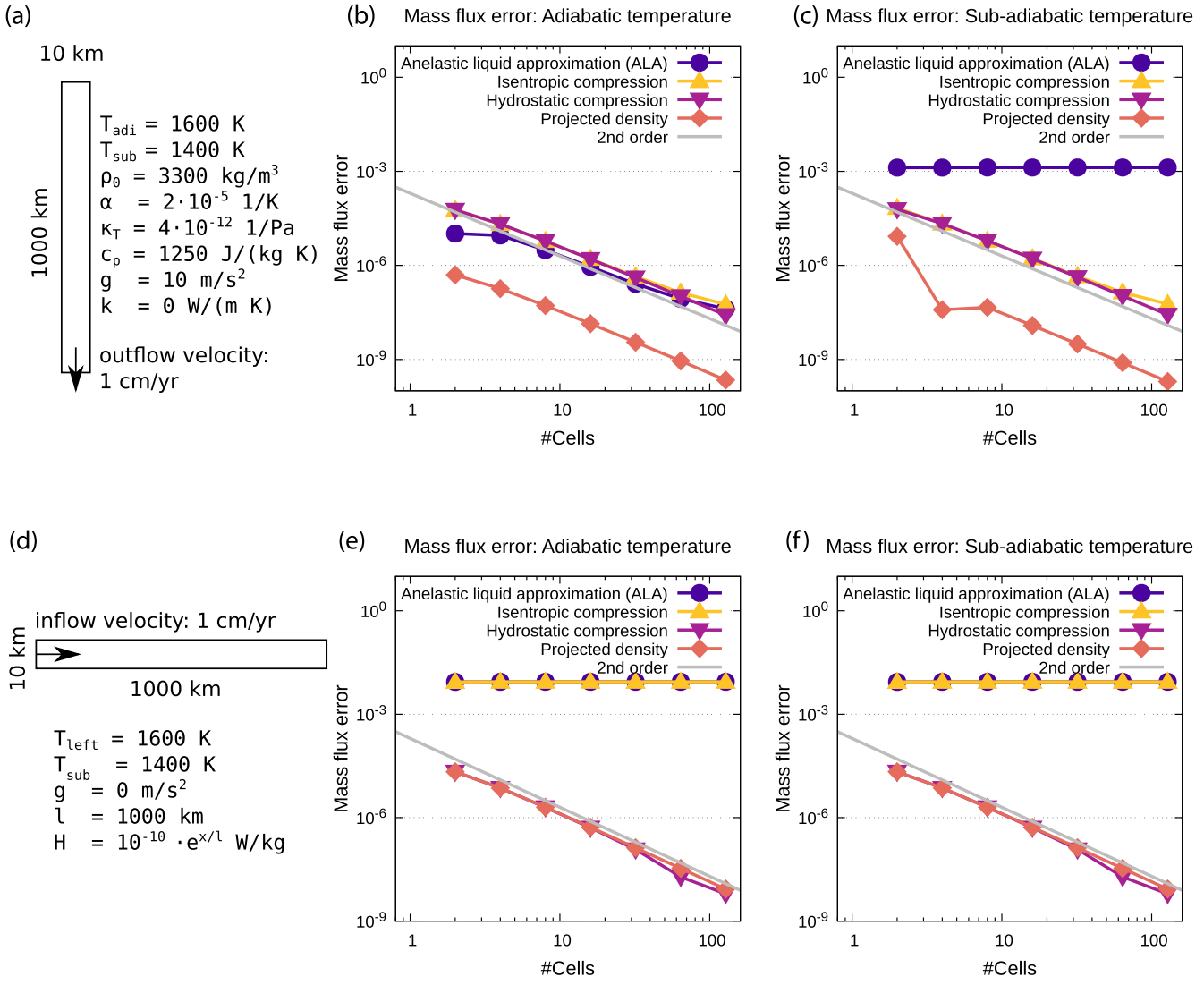

Figure 2. Model setup and mass flux error for the different compressibility approximations in the steady-state 1-D compressible pipe flow tests. The relative error is computed as $|J_{\mathrm{m,out}} + J_{\mathrm{m,in}}|/|J_{\mathrm{m,in}}|$, where $J_{\mathrm{m,in}}$ and $J_{\mathrm{m,out}}$ are the mass fluxes into and out of the model domain. Top: vertical flow test. Bottom: horizontal flow test. Left: model setup. Centre: mass flux errors if the adiabatic temperature profile matches the inflow temperature. Right: mass flux errors if the adiabatic temperature profile does not match the actual inflow temperature.

To verify this quantitatively, let us describe the setup and its model parameters that lead to a time-dependent mass outflux $J(t)$. First, we prescribe the internal heating to produce a temperature increase as

$$T(t) = T_0 + wt, \tag{26}$$

where we choose $w = 100$ K Myr^{-1}. The resulting density is then

$$\rho(t) = \rho_0 \mathrm{e}^{-\alpha(T(t)-T_0)} = \rho_0 \mathrm{e}^{-\alpha wt}. \tag{27}$$

With this setup, the (exact) outflow through the open boundary needs to exactly balance the mass change inside the model domain:

$$J_m(t) = \int_\Gamma \mathbf{n} \cdot \mathbf{j}_m(t)\,\mathrm{d}\Gamma = -\frac{\mathrm{d}}{\mathrm{d}t}\int_\Omega \rho(t)\,\mathrm{d}\Omega, \tag{28}$$

where J_m is the total mass flux, $\mathbf{j}_m$ is the mass flux density, Γ is the model boundary with normal vector $\mathbf{n}$ and Ω is the model domain. Since the density ρ is spatially uniform, we obtain

$$J_m(t) = \rho_0 w V t \mathrm{e}^{-\alpha wt}, \tag{29}$$

where V is the volume of the domain. Otherwise, we use the same material properties as in the example described in Section 3.1 and displayed in Fig. 2(a).

We show results for this situation in Fig. 3, where we use a variable number of time steps to reach a time $T = 10$ Myr and a corresponding heating of 1000 K. The equations above imply a mass flux of $J_m(T) \approx 0.0205$ kg s^{-1}. By this time, around 2 per cent of the total mass has left the model (equivalent to a 2 per cent expansion due to the increasing temperature). As expected, the mass flux can only be adequately captured by the PDA, as shown in Fig. 3(b). Its error converges as expected with the order of our BDF2 time-stepping scheme (second order), while all other approximations experience a constant model error.

As a second case, let us consider the same lateral pipe, but instead of local temperature changes we will apply a time-variable external pressure to the right model boundary. We choose the external pressure as exponentially increasing with time, leading to compression, so that material flows into the pipe from the right (Fig. 3c). The results shown in Fig. 3(d) imply that the ALA, ICA and HCA

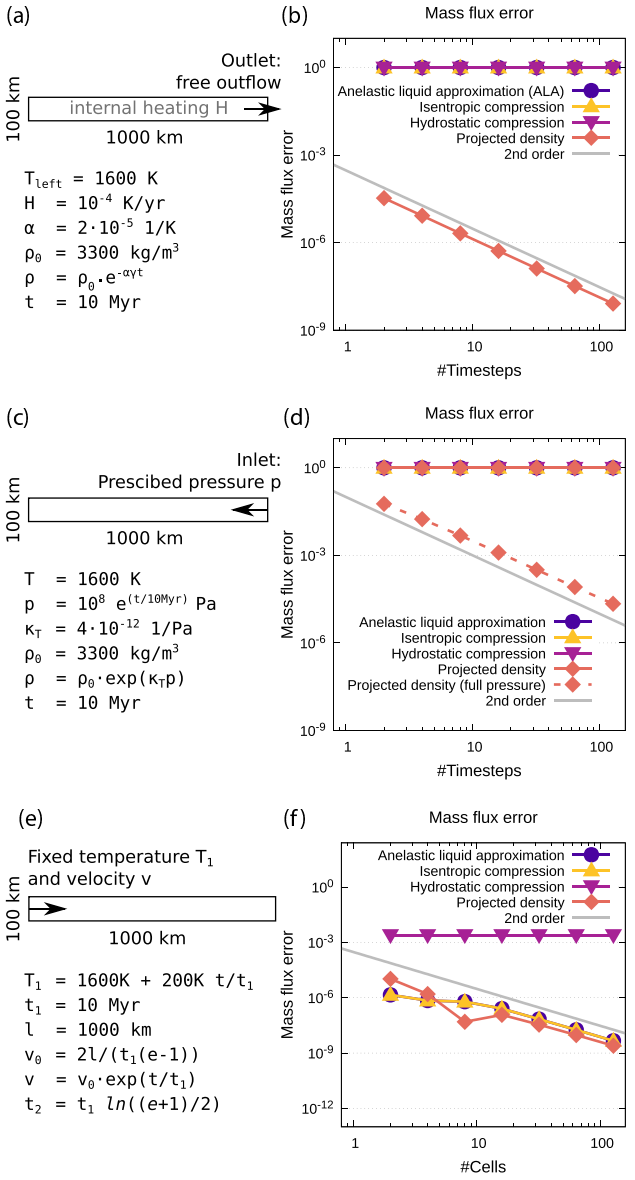

Figure 3. Time-dependent 1-D compressible pipe flow tests: model setup and relative mass flux error in $J_m(T)$ for $T = 10$ Myr for the different compressibility approximations. The error is computed as described in Fig. 2. Top row: outflow due to internal heating. Middle row: inflow due to external pressure. Bottom row: Lateral advection of a temperature gradient.

cannot be used to model this effect because they consider neither dynamic pressure nor local changes in density over time in the mass conservation equation [dynamic pressures are included only in the force balance equation (1)]. The PDA could in principle include the effect, but as discussed in Section 2.5.3, we explicitly exclude the dynamic pressure from the density calculation to prevent the generation of pressure oscillations. However, one could modify the method discussed in Section 2.5.3 to use the full, not just the hydrostatic, pressure because the solution is smooth and there are no density gradients, and therefore no pressure waves. We have made this modification and show the results with the dashed line in Fig. 3(d). The modification then correctly predicts the (small) compression of the material, and at the expected second-order convergence.

To justify our omission of the dynamic pressure component from the PDA despite the results of the previous paragraph, see our discussion of the magnitude of different density variations in Earth's mantle in Section 1.3. In the current example, a dynamic pressure change of 100 MPa changes the density by a negligible amount of 0.04 per cent.

As a third test case, we investigate the lateral advection of a density gradient. The model setup is similar to the steady-state lateral pipe flow in Section 3.1, but instead of heating the material internally over time, we fix the temperature on the left model boundary and let this temperature increase linearly over time (Fig. 3e). We also prescribe an inward material flow on the left boundary with a fixed velocity that exponentially increases over time. The right boundary is stress-free (open) so that material can flow out. Under these conditions we can derive an analytical expression for the mass flow out of the right boundary at any given time (see Appendix A). We choose to let the model evolve until the material that started at the left boundary reaches the right boundary and compare the mass flux in the model to the analytical solution.

Because all density anomalies are transported along with the flow, and there are no density changes along material pathlines, there should be no velocity divergence in this model. This is guaranteed in the ALA and ICA, because all gradients in the reference profile are vertical, while the velocity is horizontal, therefore the mass conservation equation for these approximations reduces to $\nabla \cdot \mathbf{u} = -(1/\rho)\nabla\rho \cdot \mathbf{u} = 0$.

The results shown in Fig. 3(f) point out that all approximations reproduce this result, except for the HCA, which assumes that all density gradients (including those caused by advected temperature gradients) cause a velocity divergence. Therefore, the HCA does not correctly predict the mass flux for this process, which is a considerable shortcoming, because the advection of transient density gradients due to temperature anomalies is the dominant mode of convection in the Earth. Accordingly, while HCA performs very well for steady-state advection as shown in Section 3.1, it is in fact unsuitable for transient models of mantle convection or lithosphere dynamics and we advise against using it. As in the other examples, the PDA correctly converges towards the analytic solution.

Our conclusion from this series of benchmarks is that only the PDA includes all the terms necessary to accurately solve different modes of compressible convection in geodynamic models, and that the remaining model error of using a hydrostatic reference pressure profile is at least an order of magnitude smaller than the model error of other approximations.

4 EXAMPLE APPLICATIONS

The simplified 1-D examples of the previous section show that we implemented the approximations correctly, and that capturing compressibility more accurately *could* improve the results of geodynamic models. Whether this added fidelity is actually *necessary* in typical geodynamic applications is of course an entirely different question. We will explore this question using more realistic application cases relevant for global mantle convection models, subduction zone models, and models of crustal and lithospheric deformation in the current section.

4.1 Global effects: rising plumes and sinking slabs

As shown in the previous section, when material in the mantle moves up and down along the reference temperature profile, its volume changes are computed correctly independent of the compressible

formulation. However, p–T paths of plume and slab material typically deviate by more than 100 K from the reference profile, and thermal conduction means that the paths are not isentropic (Fig. 1). The results in Section 3.1 showed that not all approximations include these effects, which causes a model error that depends on the formulation used. Here, we estimate how big this error is for typical plumes and slabs in the Earth's mantle, and how it would influence their predicted temperature, heat flux, and buoyancy.

Let us assume a plume with a relatively large excess temperature of $\Delta T_{\mathrm{CMB}} = 1000$ K when it starts at the core-mantle boundary (consistent with CMB temperature estimates of 3300–4300 K as given by Lay *et al.* 2008) that cools down to an excess temperature of $\Delta T_{\mathrm{surface}} = 250$ K as it approaches the surface. For simplicity, we also assume constant (i.e. thermodynamically inconsistent, but nevertheless representative) material properties; specifically, a thermal expansivity of $\alpha = 2 \times 10^{-5}$ K^{-1}, and densities of $\rho_{\mathrm{surface}} = 3400$ kg m^{-3} and $\rho_{\mathrm{CMB}} = 5600$ kg m^{-3}. This means that the plume has a density difference of $\Delta\rho_{\mathrm{CMB}} \approx \rho_{\mathrm{CMB}}\alpha\Delta T_{\mathrm{CMB}} = 112$ kg m^{-3}, or 2 per cent, at the core–mantle boundary, and a density difference of $\Delta\rho_{\mathrm{surface}} \approx \rho_{\mathrm{surface}}\alpha\Delta T_{\mathrm{surface}} = 17$ kg m^{-3}, or 0.5 per cent, at the surface. In other words, there is a volume decrease of about 1.5 per cent due to the plume cooling down that is not predicted in models that use a reference profile to compute the effects of compressibility. We conducted numerical models of rising plumes using these parameters and the different compressibility approximations described above, and see volume changes on the same order. This volume change is quite small compared to the volume change along the reference profile (approximately 50 per cent), and also in comparison to existing uncertainties in the material properties of the mantle.

If we do a similar estimate for subducting slabs, using $\Delta T_{\mathrm{surface}} = 1300$ K and $\Delta T_{\mathrm{CMB}} = 300$ K, the density change that is not accounted for amounts to about 2 per cent, of the same order of magnitude as found above for rising plumes. This value is consistent with previous estimates (e.g. Schubert *et al.* 2001; Ismail-Zadeh & Tackley 2010), which suggest that density variations not included in the reference profile are of the order of a few percent. Changes in heat flux and buoyancy flux are expected to be of the same order of magnitude.

In order to illustrate how these differences influence time-dependent convection in the mantle, we set up simplified geodynamic models with constant viscosity (see Table B.1 for a complete list of parameters), using the different compressibility approximations described above (Fig. 4). Temperatures are prescribed at the top and bottom boundaries, and the side boundaries are insulating. All boundaries are impermeable and allow free slip. Qualitatively, all models behave very similarly, and the differences in heat flux between the models are of the same order of magnitude as the time variability in cumulative heat flux (Fig. 4d). The main systematic difference between the models is that the timing of the onset of convection, and the growth of thermal instabilities is slightly different: Only the projected density model includes volume changes caused by thermal diffusion and the related expansion or contraction. Because cooling material decreases in volume, and heating material increases in volume, downwellings form more slowly (Figs 4a and b) and upwellings form faster than in the simulations using approximations that do not include this effect (if the heat flux across the boundary is otherwise comparable). However, this difference in the growth rate of instabilities only shifts the onset of flow by a few million years (Fig. 4c) and does not lead to large cumulative heat flux differences between the models.

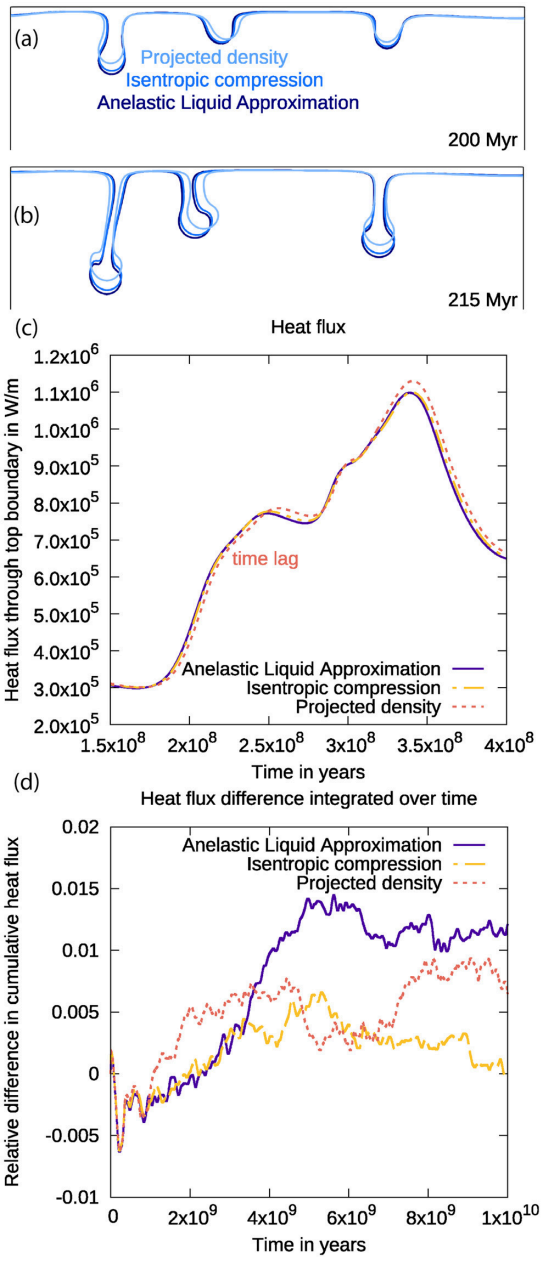

Figure 4. Simplified 2-D mantle convection model for three different compressibility approximations. (a and b) Instabilities of the upper, cold thermal boundary layer, illustrated by the blue −300 K subadiabatic temperature contours, at 200 Myr (a) and 215 Myr (b) after the start of the model. In the projected density model (light blue line), downwellings start later in time because the material contracts as it is cooled, leading to slower growth of instabilities. This time-lag is also visible in a comparison of the heat flux in the first few hundred million years between the different compressibility approximations (c). The heat flux evolution is similar in all models. There is a small time delay for the projected density model, but differences in heat flux are only of the order of a percent, even when the heat flux is integrated over time (d) and shown over a much longer time horizon. (We compute the relative difference in cumulative heat flux as $\Delta q_{\mathrm{cumulative}}(t) = \int_{\tau=0}^{t}(q - \bar{q}_{\mathrm{ICA}})\mathrm{d}\tau / \int_{\tau=0}^{t}\bar{q}_{\mathrm{ICA}}\mathrm{d}\tau$, where $\bar{q}_{\mathrm{ICA}} = \int_{\tau=0}^{10^{10}\mathrm{yrs}} q_{\mathrm{ICA}}\mathrm{d}\tau$ is the average heat flux in the model using the isentropic compression approximation and q is the heat flux in each individual model.) The differences in cumulative heat flux due to the temporal variability of each model are comparable to the heat flux differences between models due to the approximation error.

This means that for global convection models, the model error caused by using an approximation that does not include the effects of temperatures deviating from the reference profile in the mass conservation equation is so small that it can be assumed to be negligible in most cases. The effects of compositional density changes have a similar order of magnitude, and density changes due to dynamic pressures are even smaller. Only in cases where compositional density differences are much larger, such as for metal–silicate separation during core formation or the deflection of a free surface, where they can reach 100 per cent does the time derivative of the density become important (Ismail-Zadeh & Tackley 2010).

4.2 Regional effects: dynamic contraction due to phase transitions with large density changes

Some phase transitions in the mantle cause large density changes, which implies large changes in volume and consequently substantial (nonzero) values of $\nabla \cdot \mathbf{u}$. If the predominant material in the mantle undergoes the phase transition, if the density changes are not very sensitive to the chemical composition, or if the model is isochemical, these density changes can be included in the reference profiles of the ALA/TALA formulations. Examples are the transitions from olivine to wadsleyite, wadsleyite to ringwoodite and ringwoodite to bridgmanite, which are commonly included in geodynamic models. However, some phase transitions strongly depend on the chemical composition, and only a part of the material in the model would be affected. Examples include high pressure dehydration reactions, which only occur in hydrated parts of subducted slabs. These reactions can cause density changes of 20 per cent or more, and cannot be included in reference profiles, because they depend on the presence of hydrated material and the temperature of this material, which will change dynamically during the simulation.

To investigate how these phase transitions affect the dynamics and evolution of subducted slabs, and how much the model behaviour is changed if these effects are not included, we set up a simplified 2-D model of a subducting slab with a domain size of 300 km $\times$ 200 km. The slab enters the model from the top left corner, and consists of a broad cold thermal anomaly and a compositional anomaly in the form of a thin layer of hydrated crustal material. The phase transition only occurs in this top crustal layer, and the density across the phase transition changes from 2700 to 3300 kg m^{-3} at a pressure of 4 GPa (approximately 125 km depth). This roughly corresponds to the transition of antigorite serpentinite to nominally anhydrous basalt. The subduction velocity of approximately 1 cm yr^{-1} is prescribed using velocity and traction boundary conditions, and the shape and structure of the slab are determined by the temperature and composition initial and boundary conditions as detailed in Section B2. For simplicity, we chose constant material properties (except for the density), as given in Table B.1.

We show the setup and results of this model in Fig. 5. Using the full mass conservation equation, the volume of the subducted crust decreases by 20 per cent as it reaches the depth where it dehydrates. This contraction induces negative dynamic pressures and stresses whose magnitude depends on the width of the phase transition, which is approximately 5 km in our model, causing stresses of the order of 70 MPa. The magnitude of these stresses might be quite different for phase transitions in the Earth, in particular because we here use a constant viscosity and the slab is dehydrated over a very narrow depth range. However, this example illustrates that depending on the phase transition, deviatoric stresses might become large enough for brittle failure and the generation of earthquakes (e.g. Guest *et al.* 2003, 2004), in particular when considering that the negative dynamic pressure would reduce the strength of the material. If the time derivative of the density is not included in the compressibility formulation and only taken along a reference profile (such as for the classical ALA) models cannot reproduce this stress increase and volume change.

We note that the description of a dehydration phase transition as a pure contraction of the solid material as we have done in this section is of course still a simplification of the full process, which would include the emplacement and flow of the released fluid.

4.3 Regional effects: thermal contraction of a cooling crust

In the previous examples, we have discussed the effects of density changes caused by the convection of material up- or downwards within the mantle, if the density change is not included in the reference profile. But also when material is not initially moving, the conduction of heat can lead to density changes that are not correctly accounted for in the reference profile. To illustrate this effect, we use a simplified model of a thermally cooling crust.

The model setup of this example is a 2-D box with a width of 300 km and a depth of 30 km, representative of the Earth's crust. Boundary temperatures are 300 K at the top of the domain and 800 K at the bottom, and the side walls are insulating. The box is split into two areas: The right half represents old crust where the temperature increases linearly from 300 K at the surface to 800 K at a depth of 30 km (the steady-state profile when simplistically assuming pure heat conduction). The left half represents hot, recently formed crust, such as in a rift, which, for simplicity, has a constant temperature of 800 K. These areas are separated by a zone of lower viscosity that dips to the left with an angle of 45° and crosses the whole model domain from top to bottom, representative of a simplified fault zone (see also Section B3). Stress in the whole model is limited by a Drucker-Prager yield criterion, otherwise the material has a constant viscosity except for the weak fault zone separating the two regions of different temperature. The model has a deformable free surface and free-slip (zero tangential stress) boundaries at the bottom and the side walls; in other words, no externally prescribed velocities will be driving the evolution of the model.

As the hot material in the left part of the model cools, its thermal contraction causes deformation localized along the weak fault zone (see Fig. 6): The young crust in the hanging wall contracts and undergoes plastic deformation, the material close to the surface moves downwards, and a change in topography across the fault develops. In our idealized example with rather high initial lateral temperature variations, the model generates relief of ∼229 m over 5 Myr. Models using common approximations like ALA or BA—which do not include the time-derivative of the density—do not reproduce this effect (see last panels of Fig. 6).

Although not often included in geodynamic models, volumetric thermal expansion and contraction plays an important role in a number of applications, such as the generation of topography in rifts (Ziegler & Cloetingh 2004), at mid-ocean ridges (Haxby & Parmentier 1988) and on icy satellites (e.g., Mitri *et al.* 2010). Additionally, it is responsible for deformation and relief of transform faults and fracture zones close to mid-ocean ridges (Turcotte 1974; Collette 1974; Choi *et al.* 2008; Morgan *et al.* 2019), which can be illustrated as follows: As oceanic plates move away from the ridge axis, they cool and contract. Thermal contraction in the spreading direction can be compensated for by the addition of new material

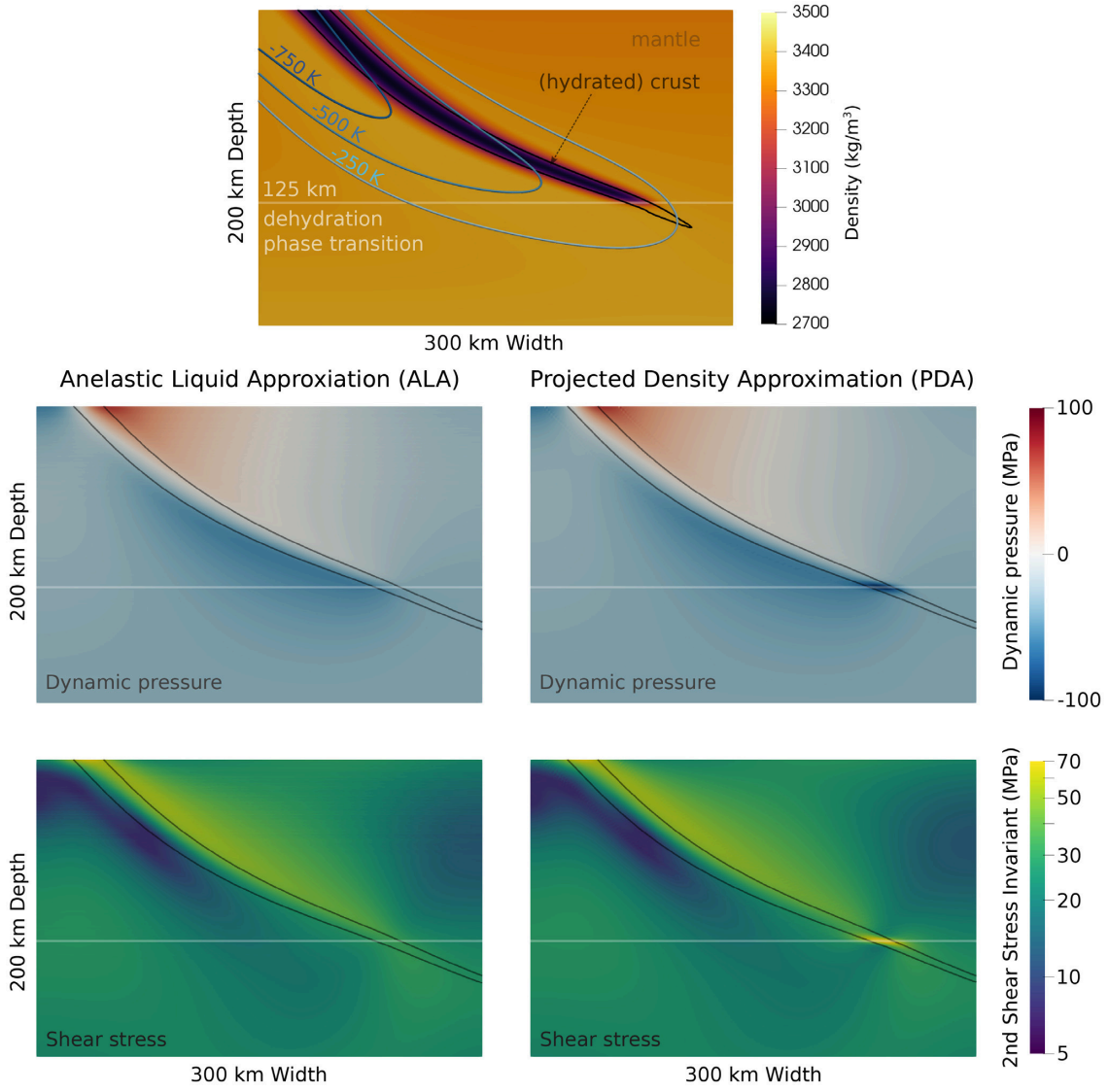

Figure 5. Top: geodynamic model of a subducted slab crossing a phase transition with a large density change, such as is common for dehydration reactions. Background colours show the density, blue contours indicate the subadiabatic temperature of the subducted slab and the black contour marks the (hydrated) crust of the slab. The phase transition occurs at a pressure of 4 GPa and is marked by a white horizontal line. It increases the density by 600kg m^{-3}, corresponding to a volume decrease of about 20 per cent. Middle and bottom: dynamic pressures and stresses as computed using the anelastic liquid approximation (left) and the full mass conservation equation (using the projected density approximation, right). Both models predict stresses induced by the flow around the subducted slab, which are of the order of 10 MPa. However, only the projected density method includes the volume change of the dehydration reaction: Because the reaction only occurs for a specific type of material (the part of the slab that is hydrated crust), it cannot be included in the reference profile. Hence, the large stresses induced by the volume reduction can only be modelled using the projected density approximation.

at the ridge axis, but contraction in ridge-parallel direction induces thermal stresses that cause deformation and lead to a widening of the transform fault valley. All of the mentioned processes are not captured in traditional compressible or incompressible formulations such as ALA and BA. Therefore, using the PDA in these applications likely improves the accuracy of the model results.

5 CONCLUSIONS

We have described and tested new, more accurate approximations of the compressible Stokes equations suitable for geodynamics, and implemented them in the open-source community modelling software ASPECT (http://aspect.geodynamics.org). Using the full mass conservation equation is possible, although it presents a challenge for numerical schemes. Instead, we propose to approximate this equation by using a density which includes the effects of changing temperature and composition, but neglects changes in dynamic pressure, which would cause volume changes of the order of 0.1 per cent or smaller. This method allows geodynamic simulations to include the time derivative of the density, capturing local changes in mass distribution without causing pressure oscillations.

Our results show that existing approximations that use a reference density profile (like the BA or the ALA) are sufficiently accurate for most global mantle convection models. However, using these common approximations neglects the effects of density changes that are not related to changes in static pressure along a specific p–T-composition trajectory, and consequently cannot be included in

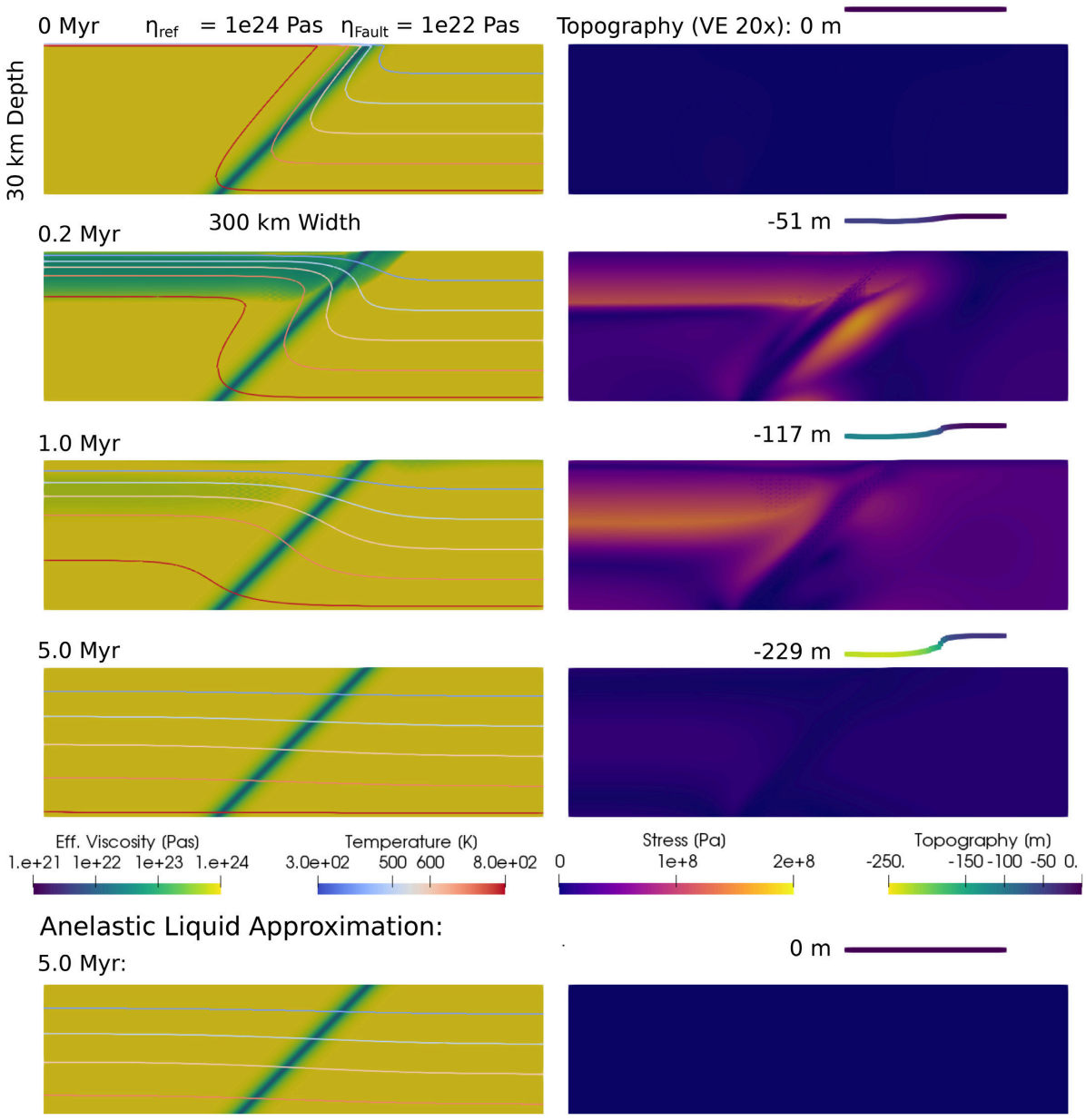

Figure 6. Top rows: idealized cooling crust model using the projected density approximation from model start to 5 Myr. Left: effective viscosity after plasticity (background colours) and temperature (isocontours) of the model evolution. Right: deviatoric stress (background colours) and topography (upper inlet, vertical exaggeration 20 ×). Bottom row: final state of an identical model setup using the anelastic liquid approximation. While the temperature evolves identically, no stress or topography is created over time.

the reference profile. For example, these effects become important in the following situations:

(i) When different types of material with different densities and phase transitions are present, and accordingly, some material undergoes phase transitions that are not included in the reference profile;
(ii) When material expands or contracts due to temperature changes caused by heat conduction close to boundary layers.

As these density changes can be of the order of 10 per cent and can happen on short timescales relative to those of viscous relaxation, they may induce substantial stresses, causing modifications to the pattern of viscous flow or even promoting plasticity or brittle failure. These consequences of induced stresses are currently not accurately represented in most numerical models, but may be crucial in studies of crustal and lithospheric deformation, e. g. for the stresses in subducting crust, or thermal cooling of rifted margins and newly created ocean floor. In cases where one wants to model these phenomena, our experiments show that only the use of the PDA can yield quantitatively accurate results.

ACKNOWLEDGEMENTS

The authors would like to thank Scott King for helpful discussions about the different approximations. We also thank Scott King and Eh Tan for their careful reviews, which greatly helped to improve this manuscript.

All authors were partially supported by the Computational Infrastructure for Geodynamics initiative (CIG), through the National Science Foundation under Award No. EAR-1550901, administered by The University of California-Davis. TH was partially supported by the National Science Foundation Award Nos. OAC-1902308 and DMS-1901529. JD, RG and WB were partially supported by the National Science Foundation under Award Nos. OCI-1148116 and OAC-1835673 as part of the Software Infrastructure for Sustained Innovation (SI2) program (now the Cyberinfrastructure for Sustained Scientific Innovation, CSSI). JD gratefully acknowledges the support of the Deep Carbon Observatory project funded by the Alfred P. Sloan Foundation. RM is funded by a UK Space Agency Aurora Postdoctoral Fellowship.

The compute time for the computations shown in Section 4 was provided by CIG on Stampede2. The authors acknowledge the Texas Advanced Computing Center (TACC, http://www.tacc.utexas.edu) at The University of Texas at Austin for providing high-performance computing resources that have contributed to the research results reported within this paper.

REFERENCES

Bangerth, W., Dannberg, J., Gassmöller, R. & Heister, T., 2016. ASPECT: Advanced Solver for Problems in Earth's ConvecTion, Computational Infrastructure in Geodynamics.

Bangerth, W., Dannberg, J., Gassmoeller, R. & Heister, T., 2018. ASPECT, v2.0.1 [software], doi:10.5281/zenodo.1244587.

Batchelor, C. & Batchelor, G., 2000. *An Introduction to Fluid Dynamics,* Cambridge Univ. Press.

Batchelor, G., 1953. The conditions for dynamical similarity of motions of a frictionless perfect-gas atmosphere, *Q. J. R. Meteorol. Soc.,* **79**(340), 224–235.

Bercovici, D., Schubert, G. & Glatzmaier, G.A., 1992. Three-dimensional convection of an infinite-Prandtl-number compressible fluid in a basally heated spherical shell, *J. Fluid Mech.,* **239,** 683–719.

Boussinesq, J., 1903. *Théorie analytique de la chaleur mise en harmonie avec la thermodynamique et avec la théorie mécanique de la lumière. Tome II: Refroidissement et échauffement par rayonnement, conductibilité des tiges, lames et masses cristallines, courants de convection, théorie mécanique de la lumière,* Vol. 2, Gauthier-Villars, Paris.

Bunge, H.-P., Richards, M.A. & Baumgardner, J.R., 1997. A sensitivity study of three-dimensional spherical mantle convection at 108 Rayleigh number: effects of depth-dependent viscosity, heating mode, and an endothermic phase change, *J. geophys. Res.,* **102**(B6), 11 991–12 007.

Choi, E.-S., Lavier, L. & Gurnis, M., 2008. Thermomechanics of mid-ocean ridge segmentation, *Phys. Earth planet. Inter.,* **171**(1–4), 374–386.

Christensen, U.R. & Yuen, D.A., 1985. Layered convection induced by phase transitions, *J. geophys. Res.,* **90**(B12), 10 291–10 300.

Collette, B.J., 1974. Thermal contraction joints in a spreading seafloor as origin of fracture zones, *Nature,* **251**(5473), 299–300.

Connolly, J., 2005. Computation of phase equilibria by linear programming: a tool for geodynamic modeling and its application to subduction zone decarbonation, *Earth planet. Sci. Lett.,* **236**(1–2), 524–541.

Curbelo, J., Duarte, L., Alboussière, T., Dubuffet, F., Labrosse, S. & Ricard, Y., 2019. Numerical solutions of compressible convection with an infinite Prandtl number: comparison of the anelastic and anelastic liquid models with the exact equations, *J. Fluid Mech.,* **873,** 646–687.

Dziewonski, A.M. & Anderson, D.L., 1981. Preliminary reference earth model, *Phys. Earth planet. Inter.,* **25**(4), 297–356.

Glatzmaier, G.A., 1988. Numerical simulations of mantle convection: Time-dependent, three-dimensional, compressible, spherical shell, *Geophys. Astrophys. Fluid Dyn.,* **43**(2), 223–264.

Gough, D., 1969. The anelastic approximation for thermal convection, *J. Atmos. Sci.,* **26**(3), 448–456.

Guest, A., Schubert, G. & Gable, C.W., 2003. Stress field in the subducting lithosphere and comparison with deep earthquakes in Tonga, *J. geophys. Res.,* **108**(B6), doi:10.1029/2002JB002161.

Guest, A., Schubert, G. & Gable, C., 2004. Stresses along the metastable wedge of olivine in a subducting slab: possible explanation for the Tonga double seismic layer, *Phys. Earth planet. Inter.,* **141**(4), 253–267, Structure and tectonics of convergent plate margins.

Haxby, W.F. & Parmentier, E., 1988. Thermal contraction and the state of stress in the oceanic lithosphere, *J. geophys. Res.,* **93**(B6), 6419–6429.

He, Y., Puckett, E.G. & Billen, M.I., 2017. A discontinuous Galerkin method with a bound preserving limiter for the advection of non-diffusive fields in solid earth geodynamics, *Phys. Earth planet. Inter,* **263,** 23–37.

Heister, T., Dannberg, J., Gassmöller, R. & Bangerth, W., 2017. High accuracy mantle convection simulation through modern numerical methods–II: realistic models and problems, *Geophys. J. Int.,* **210**(2), 833–851.

Ismail-Zadeh, A. & Tackley, P., 2010. *Computational Methods for Geodynamics,* Cambridge Univ. Press.

Ita, J. & King, S.D., 1994. Sensitivity of convection with an endothermic phase change to the form of governing equations, initial conditions, boundary conditions, and equation of state, *J. geophys. Res.,* **99**(B8), 15 919–15 938.

Jarvis, G.T. & McKenzie, D.P., 1980. Convection in a compressible fluid with infinite Prandtl number, *J. Fluid Mech.,* **96**(3), 515–583.

King, S.D., Lee, C., van Keken, P.E., Leng, W., Zhong, S., Tan, E., Tosi, N. & Kameyama, M.C., 2010. A community benchmark for 2-D Cartesian compressible convection in the Earth's mantle, *Geophys. J. Int.,* **180,** 73–87.

Kronbichler, M., Heister, T. & Bangerth, W., 2012. High accuracy mantle convection simulation through modern numerical methods, *Geophys. J. Int.,* **191,** 12–29.

Lay, T., Hernlund, J. & Buffett, B.A., 2008. Core–mantle boundary heat flow, *Nat. Geosci.,* **1**(1), 25–32.

Leng, W. & Zhong, S., 2010. Surface subsidence caused by mantle plumes and volcanic loading in large igneous provinces, *Earth planet. Sci. Lett.,* **291**(1–4), 207–214.

Mitri, G., Bland, M.T., Showman, A.P., Radebaugh, J., Stiles, B., Lopes, R., Lunine, J.I. & Pappalardo, R.T., 2010. Mountains on Titan: modeling and observations, *J. geophys. Res.,* **115**(E10), doi:10.1029/2010JE003592.

Morgan, J., de Monserrat, A., Wessel, P. & Parmentier, M., 2019. On the origin of transform fault and fracture zone deformation and relief, in *EGU General Assembly Conference Abstracts,* Vol. 21, EGU2019-5981.

Nakagawa, T. & Tackley, P.J., 2004. Effects of a perovskite–post perovskite phase change near core–mantle boundary in compressible mantle convection, *Geophys. Res. Lett.,* **31**(16), doi:10.1029/2008GC002280.

Nakagawa, T., Tackley, P.J., Deschamps, F. & Connolly, J.A., 2009. Incorporating self-consistently calculated mineral physics into thermochemical mantle convection simulations in a 3-D spherical shell and its influence on seismic anomalies in Earth's mantle, *Geochem. Geophys. Geosyst.,* **10**(3), doi:10.1029/2008GC002280.

Oberbeck, A., 1879. Über die Wärmeleitung der Flüssigkeiten bei Berücksichtigung der Strömungen infolge von Temperaturdifferenzen, *Ann. Phys.,* **243**(6), 271–292.

Ogura, Y. & Phillips, N.A., 1962. Scale analysis of deep and shallow convection in the atmosphere, *J. Atmos. Sci.,* **19**(2), 173–179.

Oxburgh, E. & Turcotte, D., 1978. Mechanisms of continental drift, *Rep. Prog. Phys.,* **41**(8), 1249, doi:10.1088/0034-4885/41/8/003.

Rayleigh, L., 1916. LIX. On convection currents in a horizontal layer of fluid, when the higher temperature is on the under side, *Lond., Edinburgh, Dublin Phil. Mag. J. Sci.,* **32**(192), 529–546.

Schubert, G., Turcotte, D.L. & Olson, P., 2001. *Mantle Convection in the Earth and Planets, Part 1,* Cambridge Univ. Press.

Steinbach, V., Hansen, U. & Ebel, A., 1989. Compressible convection in the earth's mantle: a comparison of different approaches, *Geophys. Res. Lett.,* **16**(7), 633–636.

Stixrude, L. & Lithgow-Bertelloni, C., 2005. Thermodynamics of mantle minerals–i. physical properties, *Geophys. J. Int.,* **162**(2), 610–632.

Tackley, P.J., Stevenson, D.J., Glatzmaier, G.A. & Schubert, G., 1993. Effects of an endothermic phase transition at 670 km depth in a spherical model of convection in the Earth's mantle, *Nature*, **361**(6414), 699–704.

Tan, E. & Gurnis, M., 2007. Compressible thermochemical convection and application to lower mantle structures, *J. geophys. Res.*, **112**(B6), doi:10.1029/2006JB004505.

Turcotte, D., 1974. Are transform faults thermal contraction cracks?, *J. geophys. Res.*, **79**(17), 2573–2577.

Xu, W., Lithgow-Bertelloni, C., Stixrude, L. & Ritsema, J., 2008. The effect of bulk composition and temperature on mantle seismic structure, *Earth planet. Sci. Lett.*, **275**(1–2), 70–79.

Yuen, D.A., Quareni, F. & Hong, H.-J., 1987. Effects from equation of state and rheology in dissipative heating in compressible mantle convection, *Nature*, **326**(6108), 67–69.

Ziegler, P.A. & Cloetingh, S., 2004. Dynamic processes controlling evolution of rifted basins, *Earth-Sci. Rev.*, **64**(1–2), 1–50.

APPENDIX A: DERIVATION OF THE TRANSIENT ADVECTION BENCHMARK

The general setup is explained in Section 3.2. We chose the inflow temperature and velocity as:

$$T_l(t) = 1600 + 200\frac{t}{t_1} \tag{A1}$$

$$v_x(t) = v_0 \mathrm{e}^{\frac{t}{t_1}} \tag{A2}$$

$$v_y(t) = 0. \tag{A3}$$

We call $v_x \equiv v$ and want the material in the chosen time t_1 to travel two times the length of the model l. In other words, we have the relationship

$$2l = \int_0^{t_1} v\,\mathrm{d}t = \int_0^{t_1} v_0 \mathrm{e}^{\frac{t}{t_1}}\,\mathrm{d}t = v_0 t_1(\mathrm{e}-1), \tag{A4}$$

and thus, $v_0 = \frac{2l}{t_1(\mathrm{e}-1)}$.

Further, we want the initial temperature distribution $T_0(\mathbf{x})$ to be consistent with the temperature and velocity boundary condition. Theoretically we could have chosen a constant initial temperature (the analytical result would remain unchanged), but then we would not test the numerical approximations. First we determine the equivalent time (in the past) where material that is now at location x would have been at the left boundary:

$$x(t) = \int_t^0 v\,\mathrm{d}t = \int_t^0 v_0 \mathrm{e}^{\frac{t}{t_1}}\,\mathrm{d}t = v_0 t_1 \left(1 - \mathrm{e}^{\frac{t}{t_1}}\right). \tag{A5}$$

This results in $-\frac{x(t)}{v_0 t_1} + 1 = \mathrm{e}^{\frac{t}{t_1}}$, and thus:

$$t(x) = t_1 \ln\left(1 - \frac{x}{v_0 t_1}\right) = t_1 \ln\left(1 - \frac{x(\mathrm{e}-1)}{2l}\right). \tag{A6}$$

Given this time $t(x)$ we can compute the hypothetical boundary temperature at that time in the past:

$$T_0(x) = 1600 + 200\frac{t(x)}{t_1} \tag{A7}$$

$$= 1600 + 200 \ln\left(1 - \frac{x(\mathrm{e}-1)}{2l}\right). \tag{A8}$$

Finally, we want to measure the accuracy at a time t_2 when the material that was initial at the left boundary reaches the right boundary. We can compute t_2 as follows:

$$l = \int_0^{t_2} v\,\mathrm{d}t = \int_0^{t_2} v_0 \mathrm{e}^{\frac{t}{t_1}}\,\mathrm{d}t = v_0 t_1 \left(\mathrm{e}^{\frac{t_2}{t_1}} - 1\right) \tag{A9}$$

$$= \frac{2l}{\mathrm{e}-1}(\mathrm{e}^{\frac{t_2}{t_1}} - 1). \tag{A10}$$

Some arithmetic then yields that $t_2 = t_1 \ln\left(\frac{\mathrm{e}+1}{2}\right)$.

APPENDIX B: DETAILED SETUP OF THE EXAMPLE APPLICATIONS

In order to satisfy the definitions of the thermal expansivity and the isothermal compressibility as specified in eqs (10) and (12), all application models use a density of the form

$$\rho(p, T, C) = (\rho_0 + \Delta\rho_{\mathrm{phase}}(C)) \exp(\kappa_T(p - p_0) - \alpha(T - T_0)), \tag{B1}$$

with the reference pressure $p_0 = 0$ and the reference temperature T_0 and reference density ρ_0 given in Table B.1. $\Delta\rho_{\mathrm{phase}}(C)$ describes the dependence of density on the prevalent mineral phase, which depends on the composition.

B1 Global convection model: Initial and boundary conditions

The model starts from an adiabatic temperature profile, computed from the parameters in Table B.1. To guarantee that upwellings and downwellings will initiate at the same position in the different models, we add small Gaussian temperature perturbations,

$$T(t=0) = T_{\mathrm{adi}} + \Delta T_1 \exp\left(-\frac{(x-x_1)^2}{2c_x^2} - \frac{(y-h)^2}{2c_y^2}\right) + \Delta T_2 \exp\left(-\frac{(x-x_2)^2}{2c_x^2} - \frac{(y-h)^2}{2c_y^2}\right),$$

with $\Delta T_1 = 5$ K, $\Delta T_2 = 3$ K, $x_1 = 200$ km, $x_2 = 3500$ km, $c_x = 400$ km, $c_y = 200$ km, and the height of the model domain $h = 3000$ km. To drive convection, we prescribe a temperature of 273 K at the top and 3700 K at the bottom throughout the model evolution. There is no internal heat production, but the model includes adiabatic heating and shear heating. The side boundaries are insulating, and all boundaries are impermeable and permit free slip.

B2 Dynamic contraction due to phase transitions with large density changes: initial and boundary conditions

To guarantee a steady downward flow, we prescribe both components of the velocity at the surface as $\mathbf{u} = (u_0; -u_0)$, and the horizontal component of the velocity at all other boundaries as $u_x = u_0$, with $u_0 = 1$ cm yr^{-1}. This causes an inward flow from the top left corner, angled downwards by 45°. All remaining velocity components are not fixed; instead the lithostatic pressure is applied as the vertical component of the boundary traction at the left, right and bottom boundaries, allowing for outflow at the right and bottom boundaries. The initial temperature is constant, except for a negative Gaussian anomaly in the top left corner:

$$T(t=0) = 1600\ \mathrm{K} - 1000\ \mathrm{K} \exp\left(-\frac{(y-y_0)^2 + (x-x_0)^2)}{2c^2}\right),$$

with $y_0 = 200$ km, $x_0 = 10$ km, $c = 35$ km. Throughout the model evolution, the temperature is prescribed at the left and top boundaries (where material flows in) using the same equation. The bottom and right boundaries (where material flows out) are Neumann boundaries for the temperature. The initial composition is uniform, without any hydrated crust in the model. As the model evolves and material flows in, the composition at the top boundary is prescribed as

$$C = \begin{cases} \exp\left(-\frac{(x-c)^2}{2x_0^2}\right) & x_0 < x < 60\ \mathrm{km}, \\ 0 & \text{otherwise.} \end{cases}$$

Table B.1. Parameters for the models presented in Section 4.

Quantity	Global convection model	Phase transition model	Cooling crust model
η	10^{22} Pa s	10^{22} Pa s	10^{24} Pa s
$\partial\eta/\partial T$	0	0	0
ρ_0	3300 kg m^{-3}	3300 kg m^{-3}	2800 kg m^{-3}
α	$2 \times 10^{-5} \exp(\alpha' p)$ K^{-1}	2×10^{-5} K^{-1}	4×10^{-5} K^{-1}
α'	$-1.117979 \times 10^{-11}$ Pa^{-1}	–	–
C_p	1250 J kg^{-1} K^{-1}	1250 J kg^{-1} K^{-1}	750 J kg^{-1} K^{-1}
T_0	1600 K	1600 K	800 K
$\Delta\rho_{\text{phase}}$	0	see Section B2	0
k	4.7 W m^{-1} K^{-1}	4.7 W m^{-1} K^{-1}	2.5 W m^{-1} K^{-1}
κ_T	4×10^{-12} Pa^{-1}	3.2×10^{-12} Pa^{-1}	3.2×10^{-12} Pa^{-1}
κ_S	$\kappa_T - \frac{\alpha^2 T}{\rho C_p}$	$\kappa_T - \frac{\alpha^2 T}{\rho C_p}$	$\kappa_T - \frac{\alpha^2 T}{\rho C_p}$
X extent	6000 km	300 km	300 km
Z extent	3000 km	200 km	30 km
Resolution	23 km	1.6 km	1 km

The composition at the left (inflow) boundary is prescribed to zero; we do not prescribe anything for the composition at all other (outflow) boundaries.

In this model, the density depends on the composition as given in eq. (B1), using

$$\Delta\rho_{\text{phase}}(C) = 0.5\left(\tanh\left(\frac{p - p_{\text{ph}}}{\delta p}\right) - 1\right)\delta\rho\, C,$$

with the pressure where the phase transition occurs $p_{\text{ph}} = 4$ GPa, $\delta p = 100$ MPa and $\delta\rho = 600$ kg m^{-3}. This implies a zero Clapeyron slope, and means that the hydrated crust represented by the compositional variable C is 600 kg m^{-3} lighter than the background mantle material above the phase transition, but has the same reference density as the surrounding mantle after the dehydration reaction.

The model includes adiabatic heating and shear heating, but for simplicity, we do not take into account latent heat release or consumption at the phase transition (which may lead to additional stresses caused by the associated temperature change).

B3 Cooling crust model: rheology and initial conditions

The application featuring a cooling crust uses the following initial conditions for temperature and composition:

$$T(t=0) = 800\text{ K} - 500\text{ K}\, y/h\left(0.5 + 0.5\tanh\left(\frac{x - y - x_0}{2c}\right)\right),$$

$$C(t=0) = \exp\left(-\frac{(x - y - x_0)^2}{2c^2}\right),$$

with $x_0 = 135$ km, $c = 2.5$ km and the height of the model domain $h = 30$km. Here, the compositional variable C indicates the presence of weak material in a fault zone, and influences the viscosity as given below.

The rheologic law combines a composition-dependent, but otherwise constant viscosity with a Drucker–Prager yield criterion of the form

$$\eta_{\text{plastic}} = \min\left(\max\left(\frac{\sigma_{\text{yield}}}{2\sqrt{|\,\dot{\varepsilon}^{\text{d}}_{\text{II}}\,|}}, \eta_{\text{min}}\right), \eta_{\text{max}}\right) \text{ with yield strength}$$

$$\sigma_{\text{yield}} = C_{\text{yield}}\cos\phi + p\sin\phi,$$

$$\eta_{\text{viscous}} = \eta(1 - C) + 0.01\,\eta C,$$

$$\eta_{\text{eff}} = \min(\eta_{\text{viscous}}, \eta_{\text{plastic}}),$$

and with the cohesion $C_{\text{yield}} = 20$ MPa, the friction angle $\phi = 20°$, $\eta_{\text{min}} = 10^{21}$ Pa s, $\eta_{\text{max}} = 10^{24}$ Pa s and $\eta = 10^{24}$ Pa s. $\dot{\varepsilon}^{\text{d}}_{\text{II}}$ is the second invariant of the deviatoric strain rate, computed in 2-D as $\dot{\varepsilon}^{\text{d}} = \dot{\varepsilon} - \frac{1}{2}\dot{\varepsilon}_{\text{tr}}\mathbf{I}$, with $\dot{\varepsilon}$ being the symmetric strain rate tensor, $\dot{\varepsilon}_{\text{tr}}$ its trace, and $\mathbf{I}$ being the identity tensor. The second invariant is defined as $\dot{\varepsilon}^{\text{d}}_{\text{II}} = \dot{\varepsilon}^{\text{d}}_{00}\dot{\varepsilon}^{\text{d}}_{11} - \dot{\varepsilon}^{\text{d}}_{01}\dot{\varepsilon}^{\text{d}}_{10}$. Because the deviatoric tensor has no trace and is symmetric, this can be simplified to $\dot{\varepsilon}^{\text{d}}_{\text{II}} = -\dot{\varepsilon}^{\text{d}}_{00}\dot{\varepsilon}^{\text{d}}_{00} - \dot{\varepsilon}^{\text{d}}_{01}\dot{\varepsilon}^{\text{d}}_{01}$. The boundary conditions for the model are described in the main text, and there is no radiogenic heat production or shear heating in this model.